Highly siderophile and chalcophile element behaviour in abyssal-type and supra-subduction zone mantle: new insights from the New Caledonia ophiolite

Arianna Secchiari [1,2], Philipp Gleissner[1], Chunhui Li[3], Alexey Goncharov[4], Harry Becker[1], Delphine Bosch[5], Alessandra Montanini[2]

[1] Institut für Geologische Wissenschaften, Freie Universität Berlin, Germany,

[2] Department of Chemistry, Life Sciences and Environmental Sustainability, University of Parma, Italy,

[3] Department of Geophysics and Planetary Sciences, University of Science and Technology of China, Hefei, China,

[4] Department of Geophysics, Saint Petersburg State University

[5] Géosciences Montpellier, Université de Montpellier, France

Abstract

The New Caledonia Ophiolite hosts one of the largest obducted mantle sections worldwide, offering a unique opportunity to investigate key mantle processes. The ophiolite comprises refractory harzburgites, locally overlain by mafic-ultramafic cumulates, and minor lherzolites. Previous geochemical studies indicated that the lherzolites are akin to abyssal-type peridotites, while the harzburgites underwent

multiple melting episodes in MOR and supra-subduction zone environments, followed by late stage metasomatism.

In this work, Os isotopes, highly siderophile (HSE) and chalcophile element data are reported for the New Caledonia peridotites, in order to constrain the behaviour of these elements in abyssal-type and fore-arc mantle.

The variably serpentinised lherzolites (LOI = 6.4 - 10.7 %) yield slightly subchondritic to suprachondritic initial Os isotopic compositions ($^{187}Os/^{188}Os_i$ = 0.1273-0.1329) and subchondritic to chondritic Re/Os ratios (0.04-0.11). The gently sloping HSE patterns with increasing depletion towards Au show concentrations in the range of other lherzolites from MOR or continental setting. Sulphur contents are high and variable (202-1268 ppm), and were likely increased during serpentinisation. By contrast, Se/Te ratios and concentrations are within the range of primitive mantle (PM) values, meaning that these elements were not significantly mobilised during serpentinisation.

Although displaying homogenous petrographic and geochemical features, the harzburgites are characterised by extremely heterogeneous Re-Os and HSE compositions.

Type-A harzburgites exhibit subchondritic $^{187}Os/^{188}Os_i$ (0.1203-0.1266) and low Re/Os ratios (0.01-0.04). The strong IPGE-PPGE fractionations (Pd_N/Ir_N = 0.21-0.56), coupled with positive Pt anomalies and S-Se-Te abundances often below the detection limit, suggest high melt extraction rates, resulting in sulphide consumption and Os-Ru metal alloy stabilisation.

Type-B harzburgites possess strongly fractionated, Os-Ir-Pt poor (Os = 0.003-0.072 ng/g, Ir = 0.0015-0.079 ng/g) and Pd-Re enriched patterns, associated with chondritic to suprachondritic measured $^{187}Os/^{188}Os$ (0.127-0.153). These characters are uncommon for highly depleted mantle residues. Interaction with an oxidised component does not appear as a viable mechanism to account for the IPGE-depleted

patterns of type-B harzburgites, as calculated oxygen fugacities are close to the FMQ buffer (Log ΔFMQ= 0.35 to 0.65).

The strikingly uniform mineralogical and geochemical features displayed by both harzburgite sub-types suggest that the different HSE patterns are not linked to their recent evolution, implying that subduction-related processes were superimposed on geochemical heterogeneous mantle domains, which exerted an important control on HSE behaviour during melt extraction and post melting metasomatism.

We propose that the HSE characters of the studied peridotites reflect the presence of a highly heterogeneous mantle source with a long term (> 1 Ga) evolution, possibly linked to the Zealandia formation.

1. Introduction

Highly siderophile elements (HSE: PGE+ Au-Re) are powerful geochemical tracers that can provide useful information for a variety of mantle processes, such as mantle melting, metasomatism and melt-fluid/mantle interaction (e.g. Luguet et al., 2001, 2003, 2007; Lorand et al., 2008; Ackerman et al., 2009). However, our knowledge concerning the behaviour of HSE in mantle source rocks of primitive arc magmas and the role of the subduction zone environment on HSE partitioning (i.e. hydrous melting, melt/fluid-mantle interaction) still remains quite fragmentary. Furthermore, although abundant HSE data are now available for different types of mantle peridotites, HSE data on fore-arc peridotites are remarkably scarce (e.g. Becker and Dale, 2016).

The New Caledonia ophiolite (Peridotite Nappe) hosts one of the largest and best preserved mantle sections worldwide, providing an excellent opportunity to investigate upper mantle processes. The rock exposures are dominated by harzburgite tectonites bearing a supra-subduction zone affinity (Marchesi et al., 2009; Ulrich et

al., 2010; Pirard et al., 2013; Secchiari et al., 2020). The main geochemical and isotopic features of these rock-types reflect a complex polyphase evolution, including several melting episodes in different geodynamic settings and subduction zone metasomatism (Marchesi et al., 2009; Ulrich et al., 2010; Secchiari et al., 2020). Minor spinel and plagioclase lherzolites, with compositions similar to abyssal peridotites, occur as discrete bodies in the north-western part of the island. The lherzolites record a different history compared to the extremely refractory harzburgites, as highlighted by their different geochemical signature (Ulrich et al., 2010; Secchiari et al., 2016).

In this work, a set of fully characterised peridotites (i.e. whole rock and in situ major and trace element contents, Sr-Nd-Pb isotopes) from New Caledonia (Secchiari et al., 2016, 2019, 2020) has been used to investigate Re-Os, HSE and chalcophile element (S-Se-Te) systematics. The main aims of this work are: 1) to examine the behaviour of these elements in the lherzolites (i.e. presumed abyssal peridotites) and in the ultra-depleted harzburgites, which may represent rocks from a former supra-subduction zone mantle wedge; 2) to constrain the behaviour of HSE and chalcophile elements during subduction zone processes.

2. Geological setting and petrological background

New Caledonia is a NW–SE elongated island located in the SW Pacific region, between the eastern margin of Australia and the Vanuatu archipelago (Fig. 1a). The island represents the emerged portion of the submarine Norfolk Ridge and it is composed by a mosaic of volcanic, sedimentary and metamorphic terranes, ranging in age from Permian to Miocene (Aitchison et al., 1995; Cluzel et al., 2001, 2012; Lagabrielle et al., 2013). These terranes were amalgamated during two major tectonic events: 1) an

Early Cretaceous tectonic convergence phase (Paris, 1981) and 2) a Paleocene to Late Eocene subduction culminated in the obduction of the ophiolite. Both events were characterised by high-pressure low-temperature (HP-LT) metamorphism in connection with plate convergence. New Caledonia can be sub-divided into four main geological domains (Cluzel et al., 2001; see Fig. 1): (i) the Basement units (pre-Late Cretaceous basement and Late Coniacian-to-Late Eocene sedimentary cover), (ii) the Cenozoic HP-LT metamorphic belt, (iii) the basaltic Poya Terrane and (iv) a large slab of peridotites, named the Peridotite Nappe.

The Peridotite Nappe represents an allochtonous sheet of oceanic lithosphere belonging to the former South Loyalty basin thrust on the continental basement of the Norfolk Ridge at the end of the Eocene subduction. The emplacement of the ophiolitic nappe resulted from the failed subduction of the Norfolk Ridge tip in a NE-dipping subduction zone, which culminated in the obduction of the Loyalty subarc lithosphere ~ 34 Ma ago (Cluzel et al. 2012).

The Peridotite Nappe has an extension of about 8000 km^2 and is mostly exposed in the Massif du Sud, where a thick harzburgite–dunite unit, locally overlain by kilometre-scale lenses of mafic and ultramafic intrusives, crops out. The sequence is believed to represent a crust-mantle boundary that records the onset of the Eocene subduction in a nascent arc setting (Marchesi et al., 2009; Pirard et al., 2013; Secchiari et al., 2018). Recent geochemical studies have shown that the ultramafic intrusives (i.e. dunites and wehrlites) crystallised from variably depleted melts with island arc basalt affinity, after massive interactions with the underlying harzburgite (Marchesi et al., 2009; Pirard et al., 2013). In contrast, the mafic rocks (i.e. gabbronorites) have a cumulate origin (Marchesi et al., 2009; Pirard et al., 2013; Secchiari et al., 2018) and derive from crystallisation of primitive, non-aggregated, ultra-depleted melts showing involvement of a subduction-related component in their source (Secchiari et al., 2018).

128 The harzburgites are also exposed in the northern Tiébaghi massif (Ulrich et al., 2010)
129 or as sparse tectonic klippen in the central part of the island (e.g. Kopeto, Poya,
130 Koniambo), where exceptionally fresh peridotites display primary mineral assemblages
131 similar to the more serpentinised rocks of the Massif du Sud.
132 The New Caledonia harzburgites bear an overall ultra-depleted composition, inherited
133 from a complex multistage evolution linked to the development of the Eocene
134 subduction system (Marchesi et al., 2009; Ulrich et al., 2010; Secchiari et al., 2020).
135 Geochemical studies have proposed that the harzburgites formed by high degrees of
136 fluid-assisted melting (up to 20-25 % in a supra-subduction zone environment, see
137 Marchesi et al., 2009; Ulrich et al., 2010). More recently, the work of Secchiari et al.
138 (2020) provided further constraints on the evolution of these rock-types, tracking
139 their history from melting to late stage metasomatism. Accordingly, the harzburgites
140 underwent two partial melting episodes in the spinel stability field: a first melting
141 phase in a MOR setting (15% melting degrees), followed by hydrous melting in a
142 supra-subduction zone setting (up to 18% fluid-assisted melting). Post-melting
143 cooling and re-equilibration at lithospheric conditions was accompanied by interaction
144 with ultra-depleted slab-derived hydrous melts (Secchiari et al., 2019, 2020). These
145 metasomatic processes are testified in the harzburgites by the widespread occurrence
146 of secondary metasomatic phases (i.e. thin films of Al_2O_3-, CaO- poor orthopyroxene,
147 and low Al_2O_3 and Na_2O clinopyroxene), L-MREE and Zr-Hf bulk rock enrichments, and
148 possibly by the poorly radiogenic Nd isotopic ratios shown by some samples (Secchiari
149 et al., 2020).
150 Compared to the harzburgites from the central and the southern massifs, Tiébaghi
151 samples display a more fertile nature, as revealed by the higher bulk trace element
152 concentrations as well as by the occurrence of a small fraction (up to 4 vol.%) of
153 clinopyroxene (see Ulrich et al., 2010; Secchiari, PhD thesis).

The main geochemical and petrological features of the spinel and plagioclase lherzolites are thought to reflect moderate melt extraction degrees (8-9%) in a MOR environment, followed by refertilisation by depleted MORB-type melts, yielding plagioclase lherzolites. The main petrological and geochemical features of the lherzolites have been reported in detail by Secchiari et al. (2016).

2.1 Sample description

In this contribution, sixteen samples of peridotites fully characterised for lithophile element geochemistry (i.e. major, trace element and Sr-Nd-Pb isotope compositions) were analysed for mass fractions of all PGE, Re, Au, S, Se, Te and $^{187}Os/^{188}Os$. Detailed descriptions of the lherzolites and harzburgites, including trace element chemistry and Sr-Nd-Pb isotopes, are provided in the works of Secchiari et al. (2016) and Secchiari et al. (2019, 2020), respectively.

Lherzolite samples are from the Poum and Babouillat areas, while the harzburgites were collected from several outcrops and mine zones along the island: Yaté, Kopeto, Poya, Poro and Tiébaghi (Fig. 1b and Table 1). The lherzolites include slightly serpentinised (LOI= 6.9 - 10.7 %) spinel and plagioclase lherzolites, while the harzburgites are typically not or only weakly serpentinised (LOI = 0 – 3 %), except for samples YA1, TI1 and TI2 (LOI = 6.0 - 9.0 %).

Both lherzolites and harzburgites are low strain mantle tectonites, showing dominant porphyroclastic textures (Fig. S1a-b) and local protomylonite development. Spinel lherzolites have 7-8 vol. % clinopyroxene and display a typical abyssal-type REE signature. The plagioclase lherzolites show melt impregnation microstructures (Fig. S1b) and are slightly enriched in incompatible trace element (REE, Ti, Y, and Zr) with respect to the spinel lherzolites. Harzburgites are extremely depleted rocks, as

highlighted by the general absence of clinopyroxene (with the exception of sample TI2, where clinopyroxene is ~ 4 vol. %, Fig. S1c) and remarkably low incompatible trace element contents (Secchiari et al., 2020). The primary mantle assemblage is composed of olivine, orthopyroxene and spinel. The occurrence of thin films of metasomatic ortho- and clinopyroxene (Fig. S1d) was interpreted as resulting from percolation of small fractions of subduction-related magmas (Secchiari et al., 2019, 2020).

All the lherzolites studied here contain trace amounts of sulphides with variable size, shape and position. Sulphides in five selected samples (i.e. BA1, POU2, POU3, POU1A, BAB1B, see Table S1) were analysed for their major element chemistry composition.

Frequent interstitial sulphide grains occur as polyhedral blebs, rounded or irregular-shaped grains (Fig. S2a-d-e), generally located at olivine-orthopyroxene or at olivine-olivine grain boundaries. They range from tiny crystals (~ 60 x 30 μm) up to 300 x 100/150 μm in maximum dimensions. Enclosed sulphides hosted within large olivine porphyroclasts have been also observed. Sulphide inclusions (Fig. S2a-e) have variable size (30 to 80 μm x 60 to 150 μm) and shape, from polyhedral to spherical. Very tiny enclosed sulphide grains (~ 5-6 μm x 10 μm) have been recognised in sample POU1A.

Major element composition of the sulphide phases is relatively homogeneous (Table S1 and Fig. S2, S3), showing no significant difference among enclosed and interstitial sulphides. Chemical composition of the studied sulphides mainly fall in the field of Ni-poor (Fe/Ni=1.3-2.1) monosulphide solid solution + Liquid (Fig. S3), but Ni-rich (Fe/Ni =0.7-0.8) pentlandite, resulting from cooling and re-equilibration (Guo et al., 1999), has been also identified in four of the investigated samples (POU2, POU3, POU1A, BAB1B).

In the harzburgites, sulphide phases have not been identified, nor through petrographic observation or microprobe analyses. This is consistent with the refractory nature and the high melt extraction rates experienced by these rock-types, which prevented sulphide retention in the residual mantle source.

3. Analytical methods

3.1 HSE and chalcophile elements

Seven lherzolites and nine harzburgites (including four duplicates) have been analysed in the geochemistry laboratory at Freie Universität for HSE, S, Se, Te mass fractions in whole rocks and $^{187}Os/^{188}Os$.

Detailed procedure descriptions have been given in previous works from this laboratory (e.g. Fischer-Gödde et al., 2011; Wang et al., 2013; Wang and Becker, 2013). The methods will only be briefly summarised below.

About 2.5 g of sample powder was weighed into 90 ml quartz glass digestion vessels and spiked with mixed ^{191}Ir–^{99}Ru–^{194}Pt–^{105}Pd, ^{77}Se–^{125}Te, ^{185}Re-^{190}Os and ^{34}S solutions. Then, 5 ml 14 mol/L, N_2-bubbled HNO_3 and 2.5 ml 9 mol/L HCl were added. The vessels were immediately sealed with Teflon tape and samples were digested for 16 h at 320°C and 100 bar. After digestion, osmium was extracted from the reverse aqua regia into chloroform, back extracted into HBr (Cohen and Waters, 1996), and further purified by micro distillation from a H_2SO_4-dichromate solution into 15 μl of HBr (Birck et al., 1997)

Osmium isotopes were determined as OsO_3^- in negative mode using the Thermo Finnigan Triton TIMS, using a secondary electron multiplier. Signal intensities of the

spike isotope ^{190}Os of samples were ~ 150,000–500,000 cps. Standard runs with different amounts of Os on the filament (10 pg and 100 pg) were also run in between the studied samples, yielding an average value of 0.1139 ± 0.0002 (2 s. d., n = 24) for 100 pg loads. Two hundreds scans were collected in each measurement for high-Os samples, while at least 120-140 scans were obtained for the low-Os samples. Raw data were corrected for isobaric OsO_3^- interferences, mass fractionation using the $^{192}Os/^{188}Os$ ratio of 3.08271, contributions from the Os spike solution and blank contributions. $^{187}Os/^{188}Os$ were finally adjusted relative to the mean of the Os standard. The oxygen isotope compositions used for the oxide correction of Os oxide molecules were $^{18}O/^{16}O$ of 0.00204 and $^{17}O/^{16}O$ of 0.00037 (Nier, 1950).

About 50% of the digestion solution was used for separation of the HSE fraction and about 30% for S–Se–Te separation. Chemical separation of the HSE fraction from the matrix was performed on columns filled with 10 ml of pre-cleaned Eichrom 50W-X8 (100–200 mesh) cation exchange resin (Fischer-Gödde et al., 2011). During separation, the HSE fraction was collected in 14 ml 0.5 mol/L HCl-40 vol.% acetone mixture. After the volume of the solution has been reduced to about 2 ml it was analysed for Au, Re, Ir and Pt. In order to remove interfering Cd, the remaining solution was further purified in 0.2 mol/L HCl on 3 ml Eichrom 50W-X8 (100–200 mesh) resin. The collected solution was evaporated to near dryness and the residue was taken up in 0.28 M HNO_3 for ICP-MS analysis. The analyses were carried out using a single collector Element XR instrument. We used either a Scott-type spray chamber (Re, Ir, Pt, Au) or an Aridus-I desolvator (Ir, Ru, Pt, Rh, Pd) at an oxide formation rate of $CeO^+/Ce^+ < 0.004$.

A two-step ion exchange chromatography method was used for separation of S, Se and Te (see Wang et al., 2013). Sulphur measurements were performed on the S–Se fraction at medium mass resolution mode on the Element XR. Selenium and Tellurium were measured using a double pass Scott type glass spray chamber at low mass

257 resolution mode on the Element XR, combined with a hydride generation sample
258 introduction system by reacting the sample solution with 1 g/100 g $NaBH_4$ in 0.05
259 mol/L NaOH (see Wang et al., 2013 for details).
260 For each batch of analysis, one procedural blank has been used. Procedural blanks
261 yielded the following mean values (± 1 s.d., n = 4-5): Re = 2.5 ± 2.0 pg; Os = 0.5 ±
262 0.3 pg with $^{187}Os/^{188}Os$ ratios of 0.14 ± 0.03; Ir = 15 ± 5 pg; Ru = 45 ± 14 pg; Rh =
263 24 ± 22 pg; Pt = 23 ± 29 pg; Pd = 640 ± 330 pg; Au = 4 ± 2 pg; Te = 1.1 ± 0.8 ng;
264 Se = 2.3 ± 0.8 ng; S = 2.8 ± 0.7 μg. Samples were corrected for total procedural
265 blanks using the mean values. Blank corrections for Re are negligible for most of the
266 analysed samples (≤ 0.3 - 0.8 %), but more significant for the harzburgites (~ 4 – 8
267 %). Blank corrections for Pt and Pd are again negligible for the lherzolites (~ 0.2 – 0.3
268 %), a few percents for the harzburgites (~ 0.4 – 4 %, with the exception of KPT2,
269 KPT5 and PO3 for which the correction for Pt is ~ 11 – 36 %). Blanks of Os, Ir, Ru and
270 Rh are insignificant for most of the samples (≤ 0.4 %) but higher for the most
271 depleted harzburgites, i.e. KPT2, KPT5 (~ 2 – 7 % for Os, Ir, Rh) and PO3 (~ 9 % for
272 Os and Ir, 13 % for Rh). Blank corrections for S, Se and Te in lherzolites range
273 between 1 - 1.7 % (S - Se) and 3-6% (Te), while for the harzburgites blank
274 corrections for these elements strongly affected the obtained results (corrections ~ 10
275 – 26 % for S and up to 40 - 80% for Se and Te), given the very low measured
276 abundances.
277
278 *3.2 Oxygen fugacity*
279
280 Iron oxidation state in studied spinels was measured using the "flank method"
281 developed for the JEOL JXA-8200 electron microprobe at Freie Universität (Goncharov,
282 2018). The position shift and intensity variation of FeLα and FeLβ x-ray lines were

283 investigated using as standards a collection of nineteen natural mantle spinels
284 previously characterised by Mössbauer spectroscopy for their $Fe^{3+}/\Sigma Fe$ at IPGG RAS
285 (St. Petersburg, see Goncharov & Ionov, 2012; Goncharov et al., 2015).
286 The analytical procedure was similar to the experiments performed over the last
287 decades to study $Fe^{3+}/\Sigma Fe$ in mantle garnets after the "flank" approach developed by
288 Höfer and Brey (2007).
289 The flank positions for the spectrometer were obtained from the difference spectrum
290 of almandine and andradite with known iron oxidation state in the wavelength range
291 related to FeLα and FeLβ lines. The intensities at flank positions near FeLα and FeLβ
292 lines were collected as two fake elements, setting counting time at 300 s on both
293 measurements, with 3 repetitions in the core and in the rim respectively, and
294 considering 5 separate spinel grains within one thin section. Measurement conditions
295 were 15 kV and 60 nA using TAP crystal for intensities at flank positions and with the
296 remaining four spectrometers measuring chemical composition at the same spot
297 simultaneously. The studied spinels show no significant core to rime zoning in terms
298 of FeO content, Cr# and FeLβ/FeLα ratio. Averaged FeLβ/FeLα ratios for each sample
299 were used to calculate iron oxidation state of spinel using the equation with
300 coefficients obtained after investigation of the standard collection (see Table 2).
301

302 **4. Results**

303

304 *4.1 HSE and chalcophile elements in spinel and plagioclase lherzolites*

305

306 HSE and chalcophile element compositions of the New Caledonia lherzolites are
307 reported in Table 1 and displayed in Fig. 2, 3, 4. Spinel and plagioclase lherzolites are

relatively homogeneous in terms of HSE, Se, Te concentrations, abundance patterns and Os isotopic compositions, with plagioclase-bearing samples showing indistinguishable patterns from those of spinel lherzolites. The concentrations of the highly siderophile and chalcophile elements are in the range of those observed for modern abyssal and ophiolitic peridotites, displaying good correlation for Ir group PGE (IPGE, e.g., Os vs. Ir and Ir vs. Ru) and more dispersed variations for the Pt group PGE (PPGE, Fig. S4). In primitive mantle (PM) normalised concentration diagrams (Fig. 3), the lherzolites exhibit flat or gently sloping negative patterns with similar PM-normalised PGE concentrations and depletions in Au (except for sample BAB2B) and Re compared to the PGE (with the exception of POU1A and POU3 for Re). Overall, absolute contents of the PGE are similar or slightly lower than primitive mantle (PM) values (Becker et al., 2006; Fischer-Gödde et al., 2011), overlapping the field of the abyssal peridotites and peridotite tectonites from continental settings (e.g., Fig. 2 and Becker and Dale, 2016). Ru/Ir and Pd/Ir ratios are suprachondritic, as observed for other mantle lherzolites (e.g. Lorand et al., 1999; Rehkämper et al., 1999; Luguet et al., 2003; Becker et al., 2006).

Initial $^{187}Os/^{188}Os$ ratios calculated at 53 Ma (i.e. the inferred age of initial magmatism in the subduction system, e.g. Cluzel et al., 2006) vary from chondritic to slightly suprachondritic (0.1273-0.1329, Fig. 4a), corresponding to $\gamma Os_{(53Ma)}$ of 0.5 to 4.9. These values overlap with data of abyssal peridotites and orogenic peridotites, but tend to be somewhat higher than for other mantle lherzolites bearing comparable depletion degrees (Fig. 4a and 4b). $^{187}Re/^{188}Os$ ranges from subchondritic to slightly suprachondritic values (0.186-0.525, see Fig. 4c).

Se and Te are positively correlated in the lherzolites (Fig. 5a) and range between 54 - 91.3 ng/g and 7.3 - 13.8 ng/g, r espectively. Se/Te ratios (5.9-7.1) are slightly lower than the PM value and similar to the data previously obtained on depleted lherzolites

(Wang and Becker, 2013). Se and Te do not display any correlation with PGE abundances, with the exception of Te, which shows a weak correlation with Pd (Fig. 5b). S contents are high and variable (202 - 1268 μg/g) compared to unserpentinised peridotites, leading to high S/Se ratios (2703-16289, Fig 5c).

4.2 HSE and chalcophile elements in harzburgites

On the basis of HSE behaviour and Os isotopic compositions (Fig. 2, 3 and 6, Table 1), the studied harzburgites can be grouped into two different sub-types: type-A and type-B.

Type-A harzburgites (TI1, TI2, PO4 and YA1) are characterised by notably lower PGE and chalcophile elements mass fractions (Figs. 2, 4) and more fractionated patterns (Fig. 6a) compared to the lherzolites. Mass fractions of the PGE are 1.07-2.07 ng/g for Os, 0.50-1.14 ng/g for Ir, 1.53-2.52 ng/g for Ru, 0.19-0.27 ng/g for Rh, 2.42-2.70 ng/g for Pt and 0.49-0.57 ng/g for Pd. Among the sub-group A, sample YA1 displays distinct PGE abundances, showing much lower Os, Ir, Pt, Pd contents (0.55 ppb for Os, 0.30 ppb for Ir, 0.27 ppb for Pt and 0.26 ppb for Pd), with exceptions for Ru, Rh, Au and S.

HSE and chalcophile element diagrams of type-A harzburgites display fractionated patterns, with concentrations decreasing from Os towards Re. Os and Ru are enriched compared to Ir, leading to correlated suprachondritic Os/Ir and Ru/Ir ratios (Os/Ir=2.9-7.9; Ru/Ir=1.8-2.1, Fig. 4). Pt and Au generally show positive spikes, more pronounced for Au, with the exception of YA1, which displays a negative Pt anomaly. Pd contents are low (< 0.1 PM values) and constant for PO4, TI1, TI2, with Pd/Ir showing subchondritic ratios for all the studied samples. Positive correlations are observed between IPGE (Fig. 2a-b-c) and Pt-Ir (not shown), and, somewhat

surprisingly, between IPGE and the fertility indicators (i.e. Al_2O_3 and CaO, not shown). Mass fractions of Te, Se and S are low, often close to or below the detection limit, again with the exception of the harzburgite YA1.

For all type-A harzburgites, Re concentrations are very low (about 0.02 ng/g), leading to subchondritic $^{187}Re/^{188}Os$ ratios (0.045 to 0.196, the latter value also reflecting the low Os concentrations in YA1). Os isotopic compositions are subchondritic to chondritic (0.1203-0.1266, corresponding $-5 \leq \gamma_{Osi(53\ Ma)} \leq -0.1$) and do not define any correlation with $^{187}Re/^{188}Os$ or incompatible element depletion indices (i.e. Al_2O_3, see Fig. 4).

Type-B harzburgites comprise very fresh samples from Kopeto (KPT2, KPT3, KPT5), Poro (PO3) and Poya (PY1) massifs. Compared to type-A harzburgites, these samples have much lower HSE abundances and display variable and strong fractionations among PGE and more incompatible chalcophile elements (Fig. 2 and 6b). In detail, Os, Ir and Pt show positive correlations (Fig. 2) and are strongly depleted compared to Ru, Rh and Pd (Os= 0.003-0.071 ppb, Ir= 0.015-0.079 ppb, with Os/Ru=0.01-0.26 and Ru/Ir= 2.5-20). For sample PY1, Pt is enriched relative to IPGE, Rh and Pd (Pt/Rh=7.7; Pt/Pd=5.5). Pd, Re and S-Se-Te have similarly low normalised abundances, with chalcophile elements often close to or below the detection limit. Au exhibits positive spikes for PY1, KPT3 and PO3 samples and tends to be more enriched than similar incompatible chalcophile elements (i.e. Pd and Re).

Measured $^{187}Os/^{188}Os$ ratios vary from chondritic to suprachondritic (0.1273-0.1534) and are coupled with high and variable $^{187}Re/^{188}Os$ (1.62-32). Initial Os isotopic compositions calculated at 53 Ma range from depleted to slightly suprachondritic values (0.1181-0.1365, $-7 \leq \gamma Os_{(53Ma)} \leq 3$).

385 Replicate analyses of samples PY1, KPT2, KPT5, PO3 yield quite similar results for Ru
386 (< 5 % relative deviation, except for sample KPT2) and Au (~ 6% for PY1 and KPT5)
387 and acceptable results for Pt for PY1-KPT5 (11.5 - 14.0 % relative deviation). Values
388 appear much more scattered for Os and Re (RSD> 30%) and less dispersed for Rh
389 and Pd (7≤ RSD% ≤32). The relative deviation of chalcophile elements is more limited,
390 mostly < 15%.
391 The large variations of mass fractions of HSE and chalcophile elements in duplicate
392 samples reflects the very low mass fractions of these elements combined with the
393 inhomogeneity in the distribution of HSE carrier phases in gram-size quantities of rock
394 powder, an issue that has already been recognised in peridotitic rocks (e.g. Becker et
395 al., 2006; Luguet et al., 2007).
396
397 **4.3 Oxybarometry**
398
399 Results for calculations of f_{O2} using coexisting olivine, orthopyroxene and spinel (e.g.,
400 Wood, 1990, see Table 2 and Table S2) with the reaction
401 $6\ Fe_2SiO_4 + O_2 \rightarrow 3\ Fe_2Si_2O_6 + 2\ Fe_3O_4$
402 (1)
403 are given in Table 2.
404 The calculation of f_{O2} depends on the pressure and temperature of equilibrium. For
405 this study, we used olivine-spinel geothermometry (Li et al., 1995) as this
406 thermometer is based on the same elements and minerals (Fe and Mg content in
407 olivine and spinel) that are used to calculate f_{O2}. As spinel peridotites lack a good
408 barometer, in order to maximise consistency with temperatures determined with Li et
409 al. (1995) thermometer, we have assumed a pressure of 1.0 GPa.

Ferric to total iron ratios ($Fe^{3+}/\Sigma Fe$) in spinel are similar within the harzburgites, covering a limited range of values ($0.18 \leq Fe^{3+}/Fe^{3+}+Fe^{2+} \leq 0.21$, see Table 2) indicating similar f_{O2} values for the two harzburgite sub-groups (ΔlogFMQ = 0.35-0.92).

In Fig. 7a-b spinel Cr# is reported against $Fe^{3+}/\Sigma Fe$ ratio and ΔlogFMQ for the analysed samples. Literature data for mantle peridotites from different geodynamic settings (i.e. MOR and supra-subduction zone) and arc xenoliths have also been plotted for comparison. Overall, the harzburgites share remarkable similarities with supra-subduction zone peridotites from the Izu-Bonin area (Parkinson and Pearce, 1998). Slightly lower Cr# values compared to the other harzburgites are displayed by TI2 sample, which in turn falls between abyssal peridotites and arc xenoliths array (Fig. 7a).

5. Discussion

5.1 HSE and Re-Os systematics of the lherzolites

Major element composition and lithophile trace element chemistry of spinel lherzolites indicate moderately depleted compositions, inherited from moderate partial melting degrees (8-9%) of a DMM source, whereas plagioclase lherzolites originated through reactive melt percolation of spinel lherzolites by highly depleted, incremental melt fractions of a DMM source in the shallow lithosphere (Secchiari et al., 2016). In the following sections, the processes that may have affected HSE and Os isotopic signature of the New Caledonia lherzolites will be discussed: low temperature alteration, in particular serpentinisation, partial melting and the role of melt infiltration and chemical disequilibrium of the HSE in mantle rocks.

435

436 *5.1.1 Effects of serpentinisation on HSE and $^{187}Os/^{188}Os$*

437

438 Serpentinisation is a widespread process of hydrothermal alteration in ultramafic
439 lithologies. However, its influence on HSE behaviour has not been investigated with
440 much detail, despite some authors have proposed it as a possible cause for ^{187}Os
441 ingrowth and Re variations in the upper mantle (Snow and Reisberg, 1995; Walker et
442 al., 1996; Standish et al., 2002). Recent experimental studies have shown that during
443 serpentinisation the formation of secondary sulphides, Fe-Ni alloys and native metals
444 (Au-Cu) is promoted by reducing f_{O2} conditions (Klein and Bach, 2009; Foustoukos et
445 al., 2015) and thus, with the exception of Au, HSE may be retained in the host rock.
446 Comparison of partially serpentinised and unserpentinised peridotites displaying
447 similar major element features supports the notion that at least PGE ratios are not
448 significantly affected by moderate to strong serpentinisation (Becker and Dale, 2016).
449 The New Caledonia lherzolites underwent intermediate serpentinisation degrees (LOI
450 = 6.4 to 10.7 %, see paragraph 2.1 and Table 1), which had limited effects on the
451 budget of fluid immobile moderately incompatible lithophile trace elements in these
452 rocks (Secchiari et al., 2016). Notably, PGE contents and ratios in the lherzolites are
453 similar to other unaltered and serpentinised lherzolites from the modern oceans and
454 ophiolitic complexes (see Fig. 2 and 3 e.g.; Snow et al., 2000; Luguet et al., 2001,
455 2004 ; Pearson et al., 2004; Alard et al., 2005; Becker et al., 2006; Fischer-Gödde et
456 al., 2011; Becker and Dale, 2016). This observation supports the hypothesis that PGE
457 abundances are comparable in fresh and variably serpentinised ultramafic rocks
458 (Becker et al., 2006; Liu et al., 2009; Fischer-Gödde et al., 2011; Marchesi et al.,
459 2013; Becker and Dale, 2016), implying that serpentinisation results in minor changes
460 in PGE ratios.

By contrast, the possible influence of serpentinisation on Au and Re is more difficult to evaluate, as no study has systematically investigated its effect on the behaviour of the aforementioned elements. In the lherzolites from New Caledonia, Au displays similar normalised concentrations as Re and, with the exception of a few samples, both elements are depleted relative to Pd, Te and Se. Au abundances tend to be somewhat lower than abundances in other lherzolites with similar major element composition (Fig. 3). Although the compositions can be entirely explained by magmatic fractionation processes (see subsequent chapters), minor losses of Au due to hydrothermal alteration cannot be ruled out (e.g. Lorand et al., 1999). The lack of correlation with Al_2O_3 and Yb_N (not shown) could be a hint that Au abundances may have been affected by a combination of magmatic processes and serpentinisation (i.e. Fischer-Gödde et al., 2011). Rhenium is slightly depleted compared to the PGE for most of the studied lherzolites, but displays higher concentrations than other mantle lherzolites (Fig. 3). In addition, Re contents do not correlate with LOI and Re/Os ratios cover the range generally reported for moderately depleted mantle rocks. The samples with the lowest Re contents display the highest LOI values, suggesting that no significant quantities of Re were added during the interaction with seawater during serpentinisation, as also supported by the chondritic to subchondritic $^{187}Re/^{188}Os$ ratios (see Table 1).

Likewise, the chondritic to slightly suprachondritic $^{187}Os/^{188}Os$ cannot be ascribed to serpentinisation, as unrealistically high water-rock ratios ($\sim 10^3$-10^4) would be required in order to perturb the whole rock $^{187}Os/^{188}Os$ at the % level or higher (e.g. Becker and Dale, 2016). The lherzolite data also show mass fractions of Se and Te and Se/Te that are similar to values in unserpentinised lherzolites (e.g., Wang and Becker, 2013). In contrast, sulfur in most lherzolites from New Caledonia shows much

higher concentrations than typical for peridotites, which is readily explained by contamination with seawater-derived sulfur during serpentinisation.

We thus conclude that the HSE (perhaps with the exception of Au), Se, Te and Re-Os signature of the lherzolites offer no evidence to support that serpentinisation and associated reactions affected these elements in a noticeable way.

5.1.2 Partial melting and chemical disequilibrium of the HSE in the mantle

Spinel and plagioclase lherzolites exhibit comparable HSE contents and patterns, similar to other lherzolites from oceanic or continental settings that underwent low to moderate degrees of melt extraction (Fig. 2 and 3).

Partial melting has often been invoked as a possible cause for HSE and $^{187}Os/^{188}Os$ variations in mantle rocks (e.g. Reisberg and Lorand, 1995; Meisel et al., 2001). Studies of the behaviour of HSE during mantle melting and their abundances in mantle rocks have supported the hypothesis that HSE concentrations in residual peridotites result from sulphide-silicate partitioning during magmatic processes (i.e Becker and Dale, 2016; Brenan et al., 2016 and references therein). Experimental studies have also highlighted that at temperatures relevant for mantle processes sulphide liquid and, in special cases, sulphide solid solutions, coexist in equilibrium with silicate melt, olivine, pyroxenes and an Al-rich phase (e.g. Rehkämper et al., 1999; Mungall and Brenan, 2014; Brenan et al., 2016). Experimentally determined sulphide melt-silicate melt partition coefficients ($D^{sulph/sil}$) for PGE have been shown to be high and constant (10^5 to 10^6, e.g. Mungall and Brenan 2014; Brenan et al. 2016), while Au shows slightly lower $D^{sulph/sil}$ ($\sim 10^4$). Therefore, up to moderately high degrees of melting, PGE behave as compatible elements and their inter-elemental ratios remain similar as long as sulphide is present in the mantle residue (i.e. until 20-

512 25% of partial melting, depending on initial S content of the source, see Fonseca et
513 al., 2011; Mungall and Brenan, 2014). By contrast, Re is much less chalcophile
514 ($D^{sulph/sil}$~300-800, e.g. Fonseca et al., 2007; Brenan, 2008) and is expected to
515 become more quickly depleted in the residual mantle.
516 Major element compositions of the sulphide phase observed in the spinel lherzolites
517 (Table S1) are consistent with a residual origin after incongruent melting processes
518 (e.g. Bockrath et al., 2004; Ballhaus et al., 2006). The occurrence of homogeneous
519 monosulphides also suggests relatively high cooling rate after the melting event.
520 Overall, the studied lherzolites are characterised by flat to gently sloping PGE
521 patterns, with similar PM-normalised abundances, no PPGE fractionation and nearly
522 constant ratios for IPGE (i.e. Os/Ir, Ru/Ir). By contrast, Au and Re display the
523 strongest depletion. These features imply that HSE, with the exception of Au and Re,
524 exhibit a similar compatible behaviour during mantle melting, as expected for low to
525 moderate melting degrees in presence of residual sulphide melt. This observation is
526 consistent with the previous estimates obtained through geochemical modelling
527 (Secchiari et al., 2016) and with the occurrence of a residual subsolidus sulphide
528 assemblage in spinel lherzolites.
529 Although the PGE patterns are nearly flat, with only slight depletion of Pd in a few
530 samples, the depletion of Au and Re, the range of chondritic to slightly suprachondritic
531 $\gamma^{187}Os_i$ and the higher mass fractions of Se and Te compared to Re and the other HSE
532 suggest a multi-stage history of the lherzolites. Notably, $\gamma^{187}Os_i$ do not correlate with
533 mass fractions of incompatible HSE such as Re, Re/Os nor with fertility indicators (Fig.
534 4), as was observed in some other suites of lherzolites (Becker and Dale, 2016).
535 The Os isotopic signature may be a pre-existing feature of the mantle source, i.e.
536 already present before the recent melt extraction event (Secchiari et al., 2016), as
537 supported by the dispersed Os isotopes-fertility indicators trends. In addition, the

538 remarkable absence of magmatic Cu-Fe-rich sulphides (e.g. see Lorand et al., 2013)
539 argue against a recent, post-melting sulphide addition. We thus speculate that the
540 bulk HSE, Se, Te and Os isotope compositions of the lherzolites are the result of
541 partial melting event which affected a mantle source previously characterised by an
542 heterogeneous sulphide population including both residual and magmatic sulfides
543 precipitated along grain boundaries by infiltrating melts (Burton et al., 1999; Lorand
544 et al., 1999; Alard et al., 2000, 2002).
545

546 **5.2 Sulphur, Se and Te behaviour in the New Caledonia lherzolites**

547 Sulfur mass fractions are variable in the lherzolites from New Caledonia and typically
548 much higher compared to estimates of the depleted MORB mantle source (DMM ~
549 150-200 ppm, Mathez, 1976; Salters and Stracke, 2004) and unaltered lherzolites
550 (e.g., Wang and Becker, 2013). In addition, sulphur does not correlate with fertility
551 indicators (i.e. Al_2O_3), as commonly observed in unserpentinised mantle tectonites
552 (e.g., Lorand and Alard, 2010; Wang and Becker, 2013). The high S concentrations
553 and the lack of correlation with melting indicators suggest that S experienced a late
554 addition during the evolution of these rocks. Sulphur budget of mantle peridotites can
555 be strongly affected by seawater-rock interaction, because of the high sulphate
556 content of seawater, leading to precipitation of hydrothermal sulphides and sulphate
557 (Alt and Shanks, 1998). We note that the major element chemistry indicates a
558 residual origin for the sulphide phases of the lherzolites (see paragraph 4.1 and
559 5.1.2). Hydrothermal sulphides or sulphates were not identified during microprobe
560 analyses.
561 Recent geochemical works have demonstrated the role of serpentine as a sink of S
562 under various oxidation states (S^{2-}, S^{-}, S^{0} and S^{6+}, Debret et al., 2017). These
563 studies have shown that S concentrations can be anomalously high in serpentinised

peridotites (up to 1 wt.%, see Alt et al., 2003), as S can be accommodated in serpentine minerals, accounting from 60 to 100% of the sulphur budget of the peridotite (Debret et al., 2017). In situ XANES analyses have also revealed that S can be hosted in nano-phases associated with serpentine or trapped either via Si substitutions in the tetrahedra, or as a sulphate ion in the network of the tetrahedral sheet of serpentine minerals (Debret et al., 2017).

The addition of S during serpentinisation is also reflected in the high suprachondritic S/Se ratios (up to 16500) and the excellent correlation observed between S concentrations and S/Se ratios (see Fig. 5c). Despite the strong S enrichments, Se and Te display 'normal' concentrations and Se/Te ratios are in the range of other lherzolites (see Wang and Becker, 2013). These data confirm that Se-Te contents and ratios were not significantly impacted by serpentinisation, as previously observed for other peridotites that experienced low to moderate serpentinisation degrees (e.g. Wang and Becker, 2013; Marchesi et al., 2013).

Moreover, Se-Te show a good correlation between each other (Fig. 5a), implying that they are controlled by the same mineral phases. In mantle peridotites, Se can replace S as a chalcogen anion within the crystalline structure of sulphides (e.g. Bulanova et al., 1996; Hattori et al., 2002; Helmy et al., 2010) or can form Se-rich micro phases, while Tellurium, owing to its semi metal nature, tends to partition between sulphides and late exsolved micrometric tellurides (Pt, Pd, Te, As, Bi phases). The latter are thought to crystallise at low temperatures during cooling, once sulphide melt becomes saturated with respect to Te (Luguet et al., 2004; Lorand et al., 2008; Lorand and Alard, 2010). In the lherzolites, Se and Te do not correlate with melting indicators, but Te displays a rough positive correlation with Pd (Fig. 5b), which suggests that the sulphide melt-bulk silicate partition coefficient of Te should be between Se and Pd (e.g., Figs. 3, 4, 5).

5.3 Type-A harzburgites: highly siderophile element systematics of a residual sub-arc mantle section

The distinct HSE patterns and Os isotopic signature testify that the New Caledonia harzburgites recorded a different evolution compared to the northern lherzolites.

Three of the four samples belonging to the sub-group A (TI1, TI2, PO4) show similar HSE patterns and chalcophile elements depletion, suggesting that the same processes contributed to the HSE and chalcophile element budget of these rocks. The low chalcophile element concentrations, close to or below the detection limit, coupled with low Pd/Ir ratios and subchondritic $^{187}Os/^{188}Os_i$, point out that type-A harzburgites are residues after high degree of melt extraction, where sulphides melts must have been nearly completely dissolved in the coexisting silicate melt.

Experimental studies have predicted a compatible behaviour for all the PGE during mantle melting as long as the sulphide phase is retained in the peridotite (Mungall and Brenan, 2014). Depending on the initial S content of the mantle rocks, ~17-20% of melting is required for sulphide exhaustion (Fonseca et al., 2011; Mungall and Brenan, 2014). As melting proceeds, sulphides are progressively dissolved into the melt and the PGE concentrate in the residual sulphide melt (Mungall and Brenan, 2014). Assuming that chemical equilibrium is reached, subsequent melt increments should lead to a slightly increase of whole rock PGE contents, leaving elemental ratios almost constant. At the point when sulphide is completely removed, IPGE and Pt are accommodated in metallic alloys, while Re, Au and Pd mass fraction should become extremely low, as these elements are not hosted in any residual mantle phase (Mungall and Brenan, 2014). Hence, for high melting degrees, HSE abundances in the residue should reflect mineral-melt partitioning and the P-T and f_{O2}-dependent solubility of Pt and IPGE alloys in silicate melt (Fonseca et al., 2011, 2012; Mungall and Brenan, 2014; Brenan et al., 2016).

618 The IPGE-PPGE fractionation and the resolvable fractionations between specific PGE
619 displayed by the type-A harzburgites bear witness of high melt extraction degrees,
620 which resulted in the formation of a S-free mantle residue. The fractionated Os-Ir-Ru-
621 Rh segments in the HSE patterns and the positive Pt anomalies are likely carried by
622 tiny residual sulphides (i.e. laurite) and metallic alloys (Os-Ir and Pt-Ir, see Lorand et
623 al., 1999; Luguet et al., 2001, 2007). These latter are thought to precipitate from
624 sulphide melt shortly before the complete exhaustion of sulphide (Mungall and
625 Brenan, 2014) or immediately after sulphide consumption, due to f_{S2} lowering and
626 diminished metal-sulphide complexation in the silicate melt (Fonseca et al., 2012).
627 The variable but broadly systematic IPGE inter-elemental fractionation (high Os/Ir,
628 Ru/Ir and Ru/Rh) and the occurrence of positive Pt anomalies possibly suggest the
629 presence of different residual Ir-Pt alloy proportions and preferred Os-Ru retention
630 compared to Ir in the residual PGE alloys (e.g. Brenan and Andrews, 2001; Fonseca et
631 al., 2012).
632 The HSE fractionations observed for type-A harzburgites are different from HSE
633 patterns of modern harzburgites in MOR environments (Fig. 6a), as the latter are
634 characterised by flat or weakly-fractionated Os-Ir-Ru triplet, rarely displaying positive
635 Pt spikes (Snow and Schmidt, 1998; Luguet et al., 2001, 2003). By contrast, HSE
636 elemental fractionations of type-A harzburgites resemble those observed for some arc
637 xenoliths (Saha et al., 2005; Liu et al., 2015; Scott et al., 2019) or ophiolitic
638 peridotites bearing a supra-subduction zone affinity (see Büchl et al., 2002, 2004;
639 O'Driscoll et al., 2012). Notably, similar HSE fractionations have also been reported
640 for mantle xenoliths from the Chatam Islands (New Zealand, see Pearson et al.,
641 2004).
642 Accordingly, trace element geochemical modelling has shown that the extreme
643 depletion in trace element contents displayed by the New Caledonia harzburgites was
644 achieved through a polyphase evolution, including a first melting event in a mid-ocean

ridge setting, followed by fluid-assisted melting reaching clinopyroxene exhaustion in a subduction system (see Secchiari et al., 2020). Such high melting degrees are permissible in supra-subduction zone environments, where hydrous conditions at relatively low pressures can produce melt fractions substantially exceeding 20% without invoking extremely high temperature (e.g. see Ulmer, 2001). In addition, LREE and FME (Sr, Ba, Pb) enrichments coupled with variable Pb isotope compositions of the type-A harzburgites may be explained by syn- and post-melting interactions with different subduction-related components (i.e. aqueous fluids and melts originated in the forearc setting, see Secchiari et al., 2019, 2020).

We thus conclude that the HSE and chalcophile element signature displayed by TI1, TI2 and PO4 predominantly reflect high degrees of melt extraction in a supra-subduction zone environment. The positive Pt spikes suggest that Pt-rich alloys were stable in the mantle residue and were only in part dissolved in the melt during melt extraction.

The enrichments of Au are modest (0.2-1.3 ng/g Au) and may be related to fluid overprint, either from slab-derived fluids (McInnes et al., 1999; Kepezhinskas et al., 2002) or from low-T alteration, e.g. during obduction (e.g. Snow et al., 2000).

The harzburgite YA1 shows higher S and Se concentrations (Fig. 5a), which, considering the significant LOI value of 6.83 wt.%, could be related to serpentinisation and precipitation of secondary sulphides. The strongly fractionated HSE pattern and the low concentrations of the incompatible HSE (i.e. Pd, Re) indicate that the HSE budget of YA1 is also governed by melting, as for TI1, TI2 and PO4 harzburgites. The low Os, Ir and Pt concentrations, are much closer to the values reported for type-B harzburgites (see Table 1 and Fig. 5b). Sample YA1 can thus be seen as transitional between type-A and type-B sub-group.

672 **5.4 Origin of type-B harzburgites – strong depletion followed by subduction**
673 **zone metasomatism?**
674
675 Type-B harzburgites mostly occur in the central massifs, however one sample (PO3)
676 has also been identified in the eastern zone, close to the area where one type-A
677 harzburgite (PO4) was sampled. Type-B harzburgites display remarkably different HSE
678 and Re/Os behaviour compared to type-A sub-group (Fig. 2 and 6).
679 Type-B harzburgites show low abundances of incompatible chalcophile elements, i.e.
680 Pd, S, Se and Re, with values in the range of type-A harzburgites. In principle such
681 low concentrations could be reconciled with high melting degrees and sulphide
682 exhaustion in the mantle source. The strong depletion of Os, Ir and Pt, (Fig. 6b)
683 coupled with slightly subchondritic to suprachondritic $^{187}Re/^{188}Os$ (0.23 to 37) and
684 $^{187}Os/^{188}Os$ (0.1239 to 0.302) are remarkable and do not occur in residual
685 harzburgites from convecting mantle, as represented by abyssal peridotites. By
686 contrast, type-B harzburgites share some similarities with mantle xenoliths from arc
687 settings, such as low Os contents associated with chondritic to suprachondritic
688 $^{187}Os/^{188}Os$ (Brandon et al., 1996, 1999; Saha et al., 2005; Widom, 2011). These
689 features have been ascribed to interactions with subduction zone fluids (i.e. fluids
690 from subducted altered oceanic crust and/or its sedimentary cover), which may have
691 induced sulphide breakdown, locally overprinting the Os isotopic signature of the
692 mantle (Wisdom et al., 2003). Such qualitative observations have also been supported
693 by experimental works, that highlighted the critical influence of oxygen fugacity (f_{O2})
694 on sulphide and alloy stability (e.g. Andrews and Brenan, 2002; Fonseca et al., 2011,
695 2012; Mungall and Brenan, 2014). In addition, the strongly fractionated, IPGE-
696 depleted, HSE patterns of the type-B harzburgites closely resemble those observed in
697 some refractory harzburgites and replacive dunites from ophiolitic complexes that

698 underwent interaction with S-undersaturated melts (Büchl et al., 2002; Lorand et al.,
699 2004).
700 As metasomatism by subduction fluids and hydrous melts has been proposed for the
701 New Caledonia harzburgites based on isotopic and incompatible element studies, we
702 have determined oxygen fugacities on a set of five harzburgites, in order to test if the
703 HSE signature of the two sub-groups could reflect different oxygen fugacity
704 conditions.
705 As a whole, the harzburgites in our dataset bear witness of similar oxygen fugacity
706 conditions, showing no significant difference among sub-types A and B. Both groups
707 register oxygen fugacity values close to or only slightly higher than the FMQ buffer,
708 displaying a nearly horizontal trend in the Cr# vs log (f_{O2}) ΔFMQ variation diagram
709 (Fig. 7b).
710 Partial melting of a spinel peridotite source is expected to induce progressive $Fe^{3+}/\Sigma Fe$
711 lowering in the residual mantle, due to the preferential removal of Fe^{3+} in Al-rich
712 spinel and clinopyroxene during melt extraction (Woodland et al., 2006). Thus, as
713 melting proceeds and the aforementioned phases are removed from the mantle
714 assemblage, melt extraction in un-buffered conditions should result in f_{O2} lowering in
715 the residual mantle, generating negative Cr# vs. log (f_{O2}) ΔFMQ trends (e.g. Brandon
716 and Draper, 1996). However, these correlations are rarely preserved in mantle
717 peridotites, as subsequent geochemical modifications, e.g. metasomatism, tend to
718 decouple f_{O2} from melting depletion indexes. In particular, in the sub-arc region,
719 interaction of the refractory peridotite with subduction components is expected to shift
720 the oxygen fugacity state toward higher values, due to the high oxidation capacity of
721 slab-derived fluids and melts (e.g. Parkinson and Arculus, 1999; Brandon and Draper,
722 1996; Parkinson et al., 2003).
723 The subhorizontal trends observed in Fig. 7a-b, as well as the slightly oxidised f_{O2}
724 values, thus bear evidence that oxygen fugacity was modified during melting and/or

post-melting evolution of the New Caledonia harzburgites. The measured f_{O2} are similar to those observed for the less oxidised peridotites from the Izu-Bonin region, plotting at the lower end of the arc xenoliths domain (see Fig. 7b; Wood and Virgo, 1989; Brandon and Draper, 1996; Parkinson et al., 2003). Such oxygen fugacity values most likely reflect limited interaction with slab-derived fluids and melts, in agreement with the geodynamic scenario proposed for the New Caledonia archipelago and the previous geochemical models (see Secchiari et al., 2020). In fact, Eocene subduction is believed to have started close to or in correspondence of an active oceanic spreading center, where hot and young (~ 6-9 My old, Cluzel et al., 2016) lithosphere was forced to subduct. In such a context, fluid fluxes from the downgoing slab must have been limited, due to the young age of the subducted material and the intra-oceanic nature of the subduction (Cluzel et al., 2016). In addition, post melting metasomatism involved small fractions (0.5-1%) of depleted (boninitic) melts, which may have not been able to shift mantle oxidation state toward more oxidised conditions. In fact, while large oxygen fugacity variations in mantle peridotites are permissable for low Fe^{3+} contents in spinel, more and more Fe^{3+} has to be added to cause even a small increase in f_{O2} when f_{O2} approaches FMQ buffer (Woodland et al., 2006).

The similar f_{O2} values registered by the two harzburgite sub-types attest that HSE behaviour was not critically influenced by different oxygen fugacity conditions. This observation supports the hypothesis that the two types of patterns are not directly linked to a specific process (i.e. higher melt extraction or enrichment degree or interaction with an oxidised component). Rather, the occurrence of two distinct patterns in the harzburgites may reflect an effect of source-control on the HSE behaviour during the recent evolution, indicating the presence of geochemically heterogeneous mantle domains below the New Caledonia archipelago before Eocene subduction.

752

753 **5.5 Type-B harzburgites: a broader perspective**

754

755 Despite being similar in terms of chemistry or mineralogy, type-A and B harzburgites
756 possess distinct HSE signatures. In addition, the HSE signatures of type-B harzbugites
757 have not yet been identified in other mantle tectonites, either from modern oceanic
758 lithosphere or ophiolitic complex.
759 However, similar compositions have been recently reported for some moderately
760 depleted to highly refractory peridotites and mantle xenoliths from New Zealand
761 (Scott et al., 2019). The New Zealand mantle is composed of isotopically
762 heterogeneous mantle fragments with evolutionary histories extending over 2.75 Ga
763 (Os model ages= 0.1-2.75 Ga, with a broad peak at 1.2 Ga), and PGE systematics
764 decoupled from major element compositions (see Scott et al., 2019; Liu et al., 2015).
765 These features have been explained by accretion of Zealandia lithospheric mantle
766 from amalgamation of genetically unrelated convecting mantle fragments which were
767 swept together beneath the Gondwana subduction margin, variably re-melted and
768 laterally accreted (Scott et al., 2019).
769 Among the New Zealand peridotite suites, mantle xenoliths from Lake Moana and
770 Chatam Island show HSE patterns that are similar to our dataset (Fig. 8). Lake Moana
771 Cretaceous xenoliths include cpx-free harzburgites that experienced up to 30%
772 melting, while Eocene-aged Chatam Island harzburgites exhibit a less refractory
773 nature, as attested by the presence of primary clinopyroxene (up to 1.8% modal,
774 Scott et al., 2016). Such depletion degrees were achieved either by plume melting or
775 hydrous melting in an arc setting for the Lake Moana xenoliths, whereas Chatam
776 Island samples are thought to represent fragments of fore-arc lithophere (Scott et al.,
777 2016, 2019).

778 Overall, HSE diagrams highlight that New Zealand mantle xenoliths reproduce with
779 good approximation both patterns observed in our harzburgites, namely type-A and
780 type-B (Fig. 8). IPGE patterns are broadly sub-parallel, with the New Caledonia
781 harzburgites falling within or at the lower range of values displayed by the New
782 Zealand samples, whereas Pt, Pd and Re exhibit greater variability.
783 For most of the New Zealand xenoliths, Ru concentrations are higher compared to the
784 contents in the New Caledonia harzburgites. Higher Ru contents cannot be ascribed to
785 different degrees of melting, as fertility indicators (i.e. Mg#(Ol), Cr#(Spl)) indicate
786 comparable depletion degrees for both peridotite suites (see Scott et al., 2016, 2019;
787 Secchiari et al., 2020). The increased Ru retention in the New Zealand samples may
788 be reconciled to the higher Cr-spinel content of these lithologies (up to 2.8%, see
789 Scott et al., 2016, vs. up to 0.8% for our harzburgites). Numerous studies have in
790 fact demonstrated that spinel can be a significant host for Ru ($D^{spinel/melt}$ ~ 20,
791 Capobianco and Drake, 1990). In addition, increase in oxygen fugacity markedly
792 enhances Ru compatibility in Cr-rich spinel ($D^{spinel/melt}$ up to 500 for f_{O2} of -0.5 FMQ,
793 Park et al., 2012), which can accomodate Ru within its crystal lattice (Pagé and
794 Barnes, 2016) or as laurite and/or Ru-rich alloy inclusions (Brenan and Andrews,
795 2001). Recent geochemical works have also illustrated the importance of Ru retention
796 in the sub-arc mantle for the HSE signature of arc lavas (Dale et al., 2012; Park et al.,
797 2013). These studies explain the low Ru concentrations and the high Pt/Ru ratios of
798 the volcanic products as related to Ru retention in the mantle source due to the
799 presence of Cr-rich spinel or PGM (see Dale et al., 2012; Park et al., 2013). Likewise,
800 positive Ru anomalies in our type-B harzburgites may reflect the presence of small
801 laurite or Ru-rich phase inclusions, which could have escaped the high melting
802 degrees due to the shield effect of spinel.
803 Other HSE (e.g. Pd and Re) in the New Caledonia harzburgites display a wider range
804 of values compared to the New Zealand samples.Enrichments in Pd have also been

805 recognised in other sub-arc mantle sections, where they have been attributed to slab-
806 derived fluids metasomatism, due to the high solubility of Pd in aqueous fluids
807 (McInnes et al., 1999; Park et al., 2013). Likewise, Re addition in mantle wedge
808 peridotites may be due to Re release in slab derived fluids during dehydration of the
809 mafic portion of the subducting slab (see Dale et al., 2009). Hence, we conclude that
810 Pd-Re (as well as Te-Se-S) re-enrichments in type-B harzburgites may have been
811 facilitated by minor sulphide precipitation from slab-derived fluids or melts.
812 By contrast, the widespread negative Pt anomalies may reflect destabilisation of a
813 pre-existing Pt-alloy phase, possibly related to melting after alloy saturation (see
814 Mungall and Brenan, 2016), and Pt release into the melt.
815
816 **5.6 Inferences from Re-Os systematics of the New Caledonia harzbugites**
817
818 All type-A harzburgites, including YA1, show unradiogenic $^{187}Os/^{188}Os_i$ and very low
819 Re/Os relative to the range of chondritic values (Walker et al., 2002) or primitive
820 mantle estimates (Meisel et al., 1996). The γ_{Osi} overlap with data from depleted
821 abyssal peridotites and mantle sections from some ophiolites (e.g., Becker and Dale,
822 2016).
823 In order to obtain an estimate of the time of melt depletion, we calculated Re-Os
824 model ages (T_{MA}) and Re–depletion model ages (T_{RD}). T_{RD} is generally used to estimate
825 model ages of mantle peridotites that experienced high degrees of melt extraction,
826 leading to low Re contents and low Re/Os ratios. For mantle peridotites which are
827 pure residues of high partial melting degrees sufficient to remove all Re, then T_{MA} and
828 T_{RD} ages should be identical. If a minor amount of Re remains, the two values should
829 be relatively similar, with T_{RD} providing a minimum depletion age.

The Re-depletion ages for type-A harzburgites are quite homogeneous for three of our samples (TI1, TI2, YA1) ranging between 0.4 and 0.7 Ga (see Table 1), while sample PO4 yields an older Re-depletion age of 1.3 Ga. Slightly older ages are provided by T_{MA} (0.5- 1.0 Ga for TI1, TI2, YA1 and 1.5 Ga for PO4), indicating that Re was not effectively removed after partial melting.

The younger model ages recorded by the harzburgites are likely linked to the evolution of the New Caledonia mantle in relationship to the eastern Australian margin, from which the New Caledonia archipelago was separated *via* marginal rifting about 90 Ma ago (Cluzel et al., 2001, 2012; Whattam, 2009). The ancient Re depletion age of the harzburgite PO4, on the other hand, reflects a mantle domain characterised by long-term low Re/Os ratio. This age is also mirrored by Nd isotopic signature, which shows a highly radiogenic value (ε_{Ndi} =+13.32, Secchiari et al., 2020), indicative of a mantle reservoir that underwent long-term depletion of Nd.

In addition, similar depletion ages (i.e. 1.2 Ga) occur in the New Zealand mantle rocks (see Scott et al., 2019).

These results are consistent with recent Re-Os studies on abyssal peridotites and mantle tectonites from ophiolitic sequences showing that the convecting mantle contains harzburgite domains that underwent depletion events much older than the age of peridotite processing under the ridge (e.g., Harvey et al., 2006).

In summary, the New Caledonia harzburgites show Re-Os systematics typical of depleted upper mantle, showing Early Paleozoic Os isotopic equilibration and evidence for ancient depletion events (> 1.0 Ga). This multi-stage history led to the depleted nature of the harzburgites and possibly resulted in their complex HSE geochemical signatures.

6. Summary and conclusions

A Re-Os isotopes, highly siderophile and chalcophile element investigation of the New Caledonia peridotites was carried out to unravel the behaviour of the aforementioned elements in lherzolites and harzburgites from the New Caledonia ophiolite.

The lherzolites exhibit subchondritic to slightly suprachondritic $^{187}Os/^{188}Os_i$ (0.1273-0.1329). PM-normalised HSE abundance diagrams are characterised by gently sloping patterns showing increasing depletion towards Re-Au, similar to lherzolites that experienced low to moderate melt extraction. However, the lack of correlation between HSE and fertility indicators, as well as the slightly suprachondritic Os isotopic ratios, argue against a simple partial melting history. Rather, such features and the presence of included and interstitial residual monosulphides possibly indicate that melting involved a mantle domain that has previously experienced a melt percolation event. The high S concentrations of the lherzolites (202-1268 ppm) most likely resulted from late-stage seawater-rock reactions.

By contrast, the New Caledonia harzburgites record higher degrees of melt extraction, as attested by the strikingly low, often below the detection limit, concentrations of incompatible chalcophile elements. Despite their homogeneity in terms of mineralogical and major element compositions, HSE patterns and Os isotopic compositions indicate the occurrence of two distinct harzburgite sub-groups.

Type-A harzburgites are characterised by steeply plunging HSE patterns, showing IPGE-PPGE and Os-Ir-Ru fractionation, coupled with low Re/Os ratios and subchondritic $^{187}Os/^{188}Os_i$. The strongly fractionated HSE patterns and the positive Pt anomalies, together with the high modelled melting degrees, indicate that melting occurred under hydrous conditions in sub-arc mantle.

Type-B harzburgites display notably different HSE patterns, showing depleted Os-Ir compared to Ru, positive anomalies and Pd-Re re-enrichments (relative to IPGE), coupled with chondritic to strongly suprachondritic measured Os isotopic ratios

($^{187}Os/^{188}Os$ = 0.127-0.153). These features have not been yet identified in mantle tectonites.

The similar and slightly oxidising oxygen fugacity values recorded by the two sub-types, named type-A and B, do not convincingly support the hypothesis that type-B patterns could be ascribed to massive interactions with an oxidising agent. By contrast, this observation, coupled with the uniform mineralogical and geochemical characters of the New Caledonia harzburgites, suggest that type-B patterns were not the result of a specific depletion or enrichment process related to their recent tectonic evolution in a subduction setting. Rather, these patterns could reflect the occurrence of a geochemically heterogeneous mantle source below the New Caledonia archipelago, similar to what was speculated for the New Zealand mantle. The HSE signature carried by the studied peridotites, as well as the puzzling similarity observed between the New Caledonia harzburgites and the New Zealand mantle xenoliths, might attest the presence of a mantle source bearing a long lasting evolution (> 1 Ga), possibly linked to the Zealandia formation.

Acknowledgements

The authors are grateful to M. Feth, R. Milke and D. Cluzel for help and support during clean laboratory work, microprobe analysis and sampling in New Caledonia, respectively. A.G. wishes to thank Russian Science Foundation project 17-77-10103 for supporting iron oxidation state investigations at Freie Universität of Berlin. We are indebted to Nadia Malaspina and Tiziano Catelani (University of Milano Bicocca) for providing access to SEM-EDS analyses of sulphides.

We also thank C. Bonadiman and A. Woodland for editorial handling. Constructive reviews by two anonimous reviewers are gratefully acknowledged.

This study represents a continuation of the PhD project of A.S. on the New Caledonia ophiolite, that has been supported by DFG funding (SFB-TRR 170 Subproject B2) and Italian-PRIN prot. 2015C5LN35. This work has also benefited from the equipment and framework of the COMP-HUB Initiative, funded by the 'Departments of Excellence' program of the Italian Ministry for Education, University and Research (MIUR, 2018-2022).

References

Ackerman, L., Walker, R.J., Puchtel, I.S., Pitcher, L., Jelínek, E., Strnad, L., 2009. Effects of melt percolation on highly siderophile elements and Os isotopes in subcontinental lithospheric mantle: A study of the upper mantle profile beneath Central Europe. Geochimica et Cosmochimica Acta 73, 2400–2414.

Aitchison, J.C., Clarke, L., Meffre, S., Cluzel, D., 1995. Eocene arc-continent collision in New Caledonia and implications for regional Southwest Pacific tectonic evolution. Geology 23, 161–164.

Alard, O., Luguet, A., Pearson, N.J., Griffin, W.L., Lorand, J.P., Gannoun, A., Burton, K.W., O'Reilly S.Y., 2005. In situ Os isotopes in abyssal peridotites bridge the isotopic gap between MORBs and their source mantle. Nature 436, 1005-1008.

Alt, J.C., Shanks, W.C., 1998. Sulfur in serpentinized oceanic peridotites: Serpentinization processes and microbial sulfate reduction. Journal of Geophysical Research 103, 9917–9929.

931 Alt, J.C., Shanks, W.C., 2003. Serpentinization of abyssal peridotites from the MARK
932 area, Mid-Atlantic Ridge: Sulfur geochemistry and reaction modeling. Geochimica et
933 Cosmochimica Acta 67, 641 – 653.

934 Andrews, D.R.A., Brenan, J.M., 2002. Phase-equilibrium constraints on the magmatic
935 origin of laurite + Ru–Os–Ir alloy. Canadian Mineralogist 40, 1705-1716.

936 Becker, H., Dale, C., 2016. Re–Pt–Os Isotopic and Highly Siderophile Element
937 Behavior in Oceanic and Continental Mantle Tectonites. Reviews in Mineralogy and
938 Geochemistry, 369-440

939 Becker, H., Horan, M.F., Walker, R.J., Gao, S., Lorand, J.P., Rudnick, R.L., 2006.
940 Highly siderophile element composition of the Earth ’s primitive upper mantle :
941 Constraints from new data on peridotite massifs and xenoliths. Geochimica et
942 Cosmochimica Acta 70, 4528–4550.

943 Birck, J.L., Barman, M.R., Capmas, F., 1997. Re-Os Isotopic Measurements at the
944 Femtomole Level in Natural Samples. Geostandards and Geoanalytical Research 21,
945 19–27.

946 Birner, S.K., Warren, J. M., Cottrell, E., Davis, F. A., Kelley, K. A., & Falloon, T. J.
947 (2017). Forearc peridotites from Tonga record heterogeneous oxidation of the mantle
948 following subduction initiation. Journal of Petrology, 58(9), 1755–1780.

949 Brandon, A.D., Creaser, R.A., Shirey, S.B., Carlson, R.W., 1996. Osmium recycling in
950 subduction zones. Science 272, 861– 864.

951 Brandon, A.D., Draper, D.S., 1996. Constraints on the origin of the oxidation state of
952 mantle overlying subduction zones: an example from Simcoe, Washington, USA.
953 Geochimica et Cosmochica Acta 60, 1739-1749.

954 Brandon, A.D., Norman, M.D., Walker, R.J., Morgan, J.W., 1999. 186Os–187Os
955 systematics of Hawaiian picrites. Earth and Planetary Science Letters 174, 25– 42.

956 Brandon, A.D., Snow J.E., Walker R.J., Morgan J.W., Mock, T.D., 2000. 190Pt-186Os
957 and 187Re-187Os systematics of abyssal peridotites. Earth and Planetary Science
958 Letters 177, 319-335.

959 Brenan, J.M., Andrews, D., 2001. High-temperature stability of laurite and Ru Os Ir
960 alloy and their role in PGE fractionation in mafic magmas. Canadian Mineralogist 39,
961 341–360.

962 Brenan, J.M., Bennett, N.R., Zajacz, Z., 2016. Experimental results on fractionation of
963 the highly siderophile elements (HSE) at variable pressures and temperatures during
964 planetary and magmatic differentiation. Reviews in Mineralogy and Geochemistry 81,
965 1–87.

966 Bryndzia, L.T., Wood, B.J., 1990. Oxygen thermobarometry of abyssal spinel
967 peridotites; the redox state and C-O-H volatile composition of the Earth's sub-oceanic
968 upper mantle. American Journal of Science 290, 1093–1116.

969 Brügmann, G., Batanova, V.G., Münker, C., Hofmann, A.W., 2002. Melt percolation
970 monitored by Os isotopes and HSE abundances : a case study from the mantle section
971 of the Troodos Ophiolite. Earth and Planetary Science Letters 204, 385–402.

972 Büchl, A., Brügmann, G. E., Batanova, V. G., & Hofmann, A. W., 2004. Os
973 mobilization during melt percolation: The evolution of Os isotope heterogeneities in
974 the mantle sequence of the Troodos ophiolite, Cyprus. Geochimica et Cosmochimica
975 Acta, 68, 3397-3408.

976 Bulanova, G.P., Griffin, W.L., Ryan, C.G., Shestakova, O.Y., Barnes, S.-J., 1996. Trace
977 elements in sulfide inclusions from Yakutian diamonds. Contributions to Mineralogy
978 and Petrology 124, 111–125.

979 Cluzel, D., Aitchison, J.C., Picard, C., 2001. Tectonic accretion and underplating of
980 mafic terranes in the Late Eocene intraoceanic fore-arc of New Caledonia (Southwest
981 Pacific): geodynamic implications. Tectonophysics 340, 23–59.

982 Cluzel, D., Maurizot, P., Collot, J., Sevin, B., 2012. An outline of the Geology of New
983 Caledonia ; from Permian – Mesozoic Southeast Gondwanaland active margin to
984 Cenozoic obduction and supergene evolution. Episodes 35, 72–86.

985 Cluzel, D., Meffre, S., Maurizot, P., Crawford, A.J., 2006. Earliest Eocene (53 Ma)
986 convergence in the Southwest Pacific; evidence from pre- obduction dikes in the
987 ophiolite of New Caledonia. Terra Nova 18, 395–402.

988 Cluzel, D., Ulrich, M., Jourdan, F., Meffre, S., Paquette, J.L., Audet, M.A., Secchiari,
989 A., Maurizot, P., 2016. Early Eocene clinoenstatite boninite and boninite-series dikes
990 of the ophiolite of New Caledonia; a witness of slab-derived enrichment of the mantle
991 wedge in a nascent volcanic arc. Lithos 260, 429-442.

992 Cohen, A.S., Waters, F.G., 1996. Separation of osmium from geological materials by
993 solvent extraction for analysis by thermal ionisation mass spectrometry. Analytica
994 Chimica Acta 332, 269–275.

995 Dale, C.W., Burton, K.W., Pearson, D.G., Gannoun, A., Alard, O., Argles, T.W.,
996 Parkinson, I.J., 2009. Highly siderophile element behaviour accompanying subduction
997 of oceanic crust : Whole rock and mineral-scale insights from a high-pressure terrain.
998 Geochimica et Cosmochimica Acta 73, 1394–1416.

999 Debret, B., Andreani, M., Delacour, A., Rouméjon S., Trcera, N., EIMF, Williams, H.,
1000 2017. E Assessing sulfur redox state and distribution in abyssal serpentinites using
1001 XANES spectroscopy. Earth and Planetary Science Letters 466, 1–11.

1002 Fischer-Gödde, M., Becker, H., Wombacher, F., 2011. Rhodium , gold and other highly
1003 siderophile elements in orogenic peridotites and peridotite xenoliths. Chemical
1004 Geology 280, 365–383.

1005 Fonseca, R.O.C., Mallmann, G., St.C.O'Neill, H., Campbell, I.H., 2007. How chalcophile
1006 is rhenium? An experimental study of the solubility of Re in sulphide mattes. Earth
1007 and Planetary Science Letters 260, 537–548.

1008 Fonseca, R.O.C., Mallmann, G., O'Neill, H.S., Campbell, I.H., Laurenz, V., 2011.
1009 Solubility of Os and Ir in sulfide melt: Implications for Re/Os fractionation during
1010 mantle melting. Earth and Planetary Science Letters 311, 339–350.

1011 Fonseca, R.O.C., Laurenz, V., Mallmann, G., Luguet, A., Hoehne, N., Jochum, K.P.,
1012 2012. New constraints on the genesis and long-term stability of Os-rich alloys in the
1013 the Earth's mantle. Geochimica et Cosmochimica Acta 87, 227-242.

1014 Goncharov, A.G., Ionov, D.A., 2012. Redox state of deep off-craton lithospheric
1015 mantle: New data from garnet and spinel peridotites from Vitim, southern Siberia.
1016 Contributions to Mineralogy and Petrology, 164 (5), 731-745.

1017 Goncharov, A.G., Nikitina, L.P., Borovkov, N.V., Babushkina, M.S., Sirotkin, A.N.,
1018 2015. Thermal and redox equilibrium conditions of the upper-mantle xenoliths from
1019 the Quaternary volcanoes of NW Spitsbergen, Svalbard Archipelago. Russian Geology
1020 and Geophysics, 56 (11), 1578-1602.

1021 Goncharov, A. , 2018. In-situ iron oxidation state in the upper mantle minerals using
1022 electron microprobe. Contributions to 3rd European mantle workshop. Plinius 44, p.
1023 172. DOI:10.19276/plinius.2018.03015

1024 Guo J., Griffin W. L., O'Reilly S. Y., 1999. Geochemistry and origin of sulphide
1025 minerals in mantle xenoliths: Qilin, Southeastern China. Journal of Petrology 40,
1026 1125–1149.

1027 Harvey, J., Gannoun, A., Burton, K.W., Rogers, N.W., Alard, O., Parkinson, I.J., 2006
1028 Ancient melt extraction from the oceanic upper mantle revealed by Re–Os isotopes in
1029 abyssal peridotites from the Mid-Atlantic ridge. Earth and Planetary Science Letters
1030 244, 606–621.

1031 Hattori, K.H., Arai, S., Clarke Barrie, D.B., 2002. Selenium, tellurium, arsenic and
1032 antimony contents of primary mantle sulfides. Canadian Mineralogist 40, 637–650.

1033 Helmy, H.M., Ballhaus, C., Wohlgemuth-Ueberwasser, C., Fonseca, R.O.C., Laurenz,
1034 V., 2010. Partitioning of Se, As, Sb, Te and Bi between monosulfide solid solution and
1035 sulfide melt – Application to magmatic sulfide deposits. Geochimica et Cosmochimica
1036 Acta 74, 6174–6179.

1037 Höfer H. E., Brey G. P., 2007. The iron oxidation state of garnet by electron
1038 microprobe: Its determination with the flank method combined with major-element
1039 analysis. American Mineralogist 92, 873–885.

1040 Kepezhinskas, P., Defant, M. J. and Widom, E., 2002. Abundance and distribution of
1041 PGE and Au in the island-arc mantle: implications for sub-arc metasomatism. Lithos
1042 60, 113–128.

1043 Klein, F., Bach, W., 2009. Fe–Ni–Co–O–S Phase Relations in Peridotite–Seawater
1044 Interactions. Journal of Petrology 50, 37–59.

1045 Lagabrielle, Y., Chauvet, A., Ulrich, M., Guillot, S., 2013. Passive obduction and
1046 gravity-driven emplacement of large ophiolitic sheets: The New Caledonia ophiolite
1047 (SW Pacific) as a case study? Bulletin de la Société Géologique de France 184, 545–
1048 556.

1049 Lassiter, J.C., Byerly, B.L., Snow, J.E., Hellebrand, E., 2014. Constraints from Os-
1050 isotope variations on the origin of Lena Trough abyssal peridotites and implications for
1051 the composition and evolution of the depleted upper mantle. Earth and Planetary
1052 Science Letters 403, 178–187.

1053 Lee, C.T.A., Leeman, W.P., Canil, D., Li, Z.X.A., 2005. Similar V/Sc systematics in
1054 MORB and arc basalts: Implications for the oxygen fugacities of their mantle source
1055 regions. Journal of Petrology 46, 2313–2336.

1056 Liu, C., Snow, J.E., Brügmann, G., Hellebrand, E., Hofmann, A.W., 2009. Non-
1057 chondritic HSE budget in Earth ’s upper mantle evidenced by abyssal peridotites from
1058 Gakkel ridge (Arctic Ocean). Earth and Planetary Science Letters 283, 122–132.

1059 Liu, J., Scott, J.M., Martin, C.E., Pearson, D.G., 2015. The longevity of Archean mantle
1060 residues in the convecting upper mantle and their role in young continent formation.
1061 Earth and Planetary Science Letters 424, 109–118.

1062 Lorand, J.-P., 1991. Sulphide Petrology and Sulphur Geochemistry of Orogenic
1063 Lherzolites: A Comparative Study of the Pyrenean Bodies (France) and the Lanzo
1064 Massif (Italy). Journal of Petrology Special Volume, 77–95.

1065 Lorand, J.-P., Pattou, L., Gros, M., 1999. Fractionation of Platinum-group Elements
1066 and Gold in the Upper Mantle: a Detailed Study in Pyrenean Orogenic Lherzolites.
1067 Journal of Petrology 40, 957–981.

1068 Lorand, J., Luguet, A., Alard, O., 2008. Platinum-Group Elements : A New Set of Key
1069 Tracers for the Earth's Interior. Elements 4, 247–252.

1070 Lorand, J.P., Alard, O., 2010. Determination of selenium and tellurium concentrations
1071 in Pyrenean peridotites (Ariege, France): New insight into S/Se/Te systematics of the
1072 upper in mantle samples. Chemical Geology 278, 120–130.

1073 Lorand, J.P., Alard, O., Luguet, A., Keays, R.R., 2003. Sulfur and selenium
1074 systematics of the subcontinental lithospheric mantle: Inferences from the Massif
1075 Central xenolith suite (France). Geochimica et Cosmochimica Acta 67, 4137–4151.

1076 Lorand, J.P., Delpech, G., Grégoire, M., Moine, B., O'Reilly, S.Y., Cottin, J.Y., 2004.
1077 Platinum-group elements and the multistage metasomatic history of Kerguelen
1078 lithospheric mantle (South Indian Ocean). Chemical Geology 208, 195–215.

1079 Luguet, A., Alard, O., Lorand, J.P., Pearson, N.J., Ryan, C.Y., Reilly, S.Y.O., 2001.
1080 Laser-ablation microprobe (LAM) -ICPMS unravels the highly siderophile element
1081 geochemistry of the oceanic mantle. Earth and Planetary Science Letters 189, 285–
1082 294.

1083 Luguet, A., Lorand, J.P., Seyler, M., 2003. Sulfide petrology and highly siderophile
1084 element geochemistry of abyssal peridotites : A coupled study of samples from the
1085 Kane Fracture Zone (45 ° W 23 ° 20N , MARK Area , Atlantic Ocean). Geochimica et
1086 Cosmochimica Acta 67, 1553–1570.

1087 Luguet, A., Lorand, J., Alard, O., Cottin, J., 2004. A multi-technique study of platinum
1088 group element systematic in some Ligurian ophiolitic peridotites , Italy. Chemical
1089 Geology 208, 175–194.

1090 Luguet, A., Shirey, S.B., Lorand, J.P., Horan, M.F., Carlson, R.W., 2007. Residual
1091 platinum-group minerals from highly depleted harzburgites of the Lherz massif

(France) and their role in HSE fractionation of the mantle. Geochimica et Cosmochimica Acta 71, 3082–3097.

Marchesi, C., Garrido, C.J., Godard, M., Belley, F., Ferré, E., 2009. Migration and accumulation of ultra-depleted subduction-related melts in the Massif du Sud ophiolite (New Caledonia). Chemical Geology 266, 171–186.

Marchesi, C., Garrido, C.J., Harvey, J., 2013. Platinum-group elements , S , Se and Cu in highly depleted abyssal peridotites from the Mid-Atlantic Ocean Ridge (ODP Hole 1274A): Influence of hydrothermal and magmatic processes. Contributions to Mineralogy and Petrology 166, 1521–1538.

Mathez, E.A., 1976. Sulfur solubility and magmatic sulfides in submarine basalt glass. Journal of Geophysical Research 81, 4269–4276.

McInnes, B. I. A., McBride, J. S., Evans, N. J., Lambert, D. D. & Andrew, A. S., 1999. Osmium isotope constraints on ore metal recycling in subduction zones. Science 286, 512–516.

Meisel, T., Walker, R.J., Irving, A.J., Lorand, J.-P., 2001. Osmium isotopic compositions of mantle xenoliths: a global perspective. Geochimica et Cosmochimica Acta 65, 1311–1323.

Mungall J.E., Brenan, J., 2014. Partitioning of platinum-group elements and Au between sulfide liquid and basalt and the origins of mantle-crust fractionation of the chalcophile elements. Geochimica et Cosmochimica Acta 125, 265–289.

O'Driscoll, B., Day, J.M.D., Walker, R.J., Daly, J.S., McDonough, W.F., Piccoli, P.M., 2012. Chemical heterogeneity in the upper mantle recorded by peridotites and chromitites from the Shetland Ophiolite Complex, Scotland. Earth and Planetary Science Letters 333–334, 226–237.

1116 Pagé, P., Barnes, S.-J., 2016. The influence of chromite on osmium, iridium,
1117 ruthenium and rhodium distribution during early magmatic processes. Chemical
1118 Geology 420, 51–68.

1119 Park, J., Campbell, I.H., Arculus, R.J., 2013. Platinum-alloy and sulfur saturation in an
1120 arc-related basalt to rhyolite suite : Evidence from the Pual Ridge lavas , the Eastern
1121 Manus Basin. Geochimica et Cosmochimica Acta 101, 76–95.

1122 Parkinson, I.J., Pearce, J.A., 1998. Peridotites from the Izu–Bonin–Mariana Forearc
1123 (ODP Leg 125): evidence for mantle melting and melt–mantle interaction in a supra-
1124 subduction zone setting. Journal of Petrology 9, 1577–1618.

1125 Parkinson, I.J., Arculus, R.J., Eggins, S.M., 2003. Peridotite xenoliths from Grenada,
1126 Lesser Antilles Island Arc. Contributions to Mineralogy and Petrology 146: 241–262.

1127 Pearson, D.G., Irvine, G.J., Ionov, D.A., Boyd, F.R., Dreibus, G.E., 2004. Re-Os
1128 isotope systematics and platinum group element fractionation during mantle melt
1129 extraction: A study of massif and xenolith peridotite suites. Chemical Geology 208,
1130 29–59.

1131 Pirard, C., Hermann, J., O'Neill, H.St.C., 2013. Petrology and geochemistry of the
1132 crust– mantle boundary in a nascent arc, Massif du Sud ophiolite, New Caledonia, SW
1133 Pacific. Journal of Petrology 0, 1–34.

1134 Rehkämper, M., Halliday, A.N., Alt, J., Fitton, J.G., Zipfel, J., Takazawa, E., 1999.
1135 Non-chondritic platinum-group element ratios in oceanic mantle lithosphere:
1136 petrogenetic signature of melt percolation? Earth and Planetary Science Letters 172,
1137 65–81.

1138 Reisberg, L., Lorand, J.-P., 1995. Longevity of sub-continental mantle lithosphere
1139 from osmium isotope systematics in orogenic peridotite massifs. Nature 376, 159–
1140 162.

1141 Saha, A., Basu, A.R., Jacobsen, S.B., Poreda, R.J., 2005. Slab devolatilization and Os
1142 and Pb mobility in the mantle wedge of the Kamchatka arc. Earth and Planetary
1143 Science Letters 236, 182–194.

1144 Salters, V.J.M., Stracke, A., 2004. Composition of the depleted mantle. Geochemistry
1145 Geophysics Geosystems 5 (5).

1146 Scott, J.M., Liu, J., Pearson, D.G., Harris, G.A., Czertowicz, T.A., Woodland, S.J.,
1147 Riches, A.J.V., Luth, R.W., 2019. Continent stabilisation by lateral accretion of
1148 subduction zone-processed depleted mantle residues; insights from Zealandia. Earth
1149 and Planetary Science Letters 507, 175–186.

1150 Scott, J.M., Liu, J., Pearson, D.G., Waight, T.E., 2016. Mantle depletion and
1151 metasomatism recorded in orthopyroxene in highly depleted peridotites. Chemical
1152 Geology 441, 280–291.

1153 Secchiari, A., Montanini, A., Bosch, D., Macera, P., Cluzel, D., 2020. Sr-Nd-Pb and
1154 trace element systematics of the New Caledonia harzburgites: tracking source
1155 depletion and contamination processes in a SSZ setting. In press on Geoscience
1156 Frontiers, special issue Ophiolites. https://doi.org/10.1016/j.gsf.2019.04.004

1157 Secchiari, A., Montanini, A., Bosch, D., Macera, P., Cluzel, D., 2019. Origin of the
1158 spinel-pyroxene symplectites in the harzburgites from the New Caledonia peridotite.
1159 Ofioliti 44, 31-42.

1160 Secchiari, A., Montanini, A., Bosch, D., Macera, P., Cluzel, D., 2018. The contrasting
1161 geochemical message from the New Caledonia gabbronorites: insights on depletion

and contamination processes of the sub-arc mantle in a nascent arc setting. Contributions to Mineralogy and Petrology 173, 66.

Secchiari, A., Montanini, A., Bosch, D., Macera, P., Cluzel, D., 2016. Melt extraction and enrichment processes in the New Caledonia lherzolites: evidence from geochemical and Sr–Nd isotope data. Lithos 260, 28–43.

Secchiari, A., 2016. Sr-Nd-Pb isotope investigation of the New Caledonia Ophiolite. PhD thesis, Parma and Montpellier University, 191 pp.

Snow, J.E., Reisberg, L., 1995. Os isotopic systematics of the MORB mantle: results from altered abyssal peridotites. Earth and Planetary Science Letters 133, 411–421.

Snow, J., Schmidt, G., Rampone E., 2000. Os isotopes and highly siderophile elements (HSE) in the Ligurian ophiolites, Italy. Earth and Planetary Science Letters 175, 119-132

Standish, J.J., Hart, S.R., Blusztajn, J., Dick, H.J.B., Lee, K.L., 2002. Abyssal peridotite osmium isotopic compositions from Cr-spinel. Geochemistry Geophysics Geosystems 3, (1).

Ulmer, P., 2001. Partial melting in the mantle wedge — the role of H2O in the genesis of mantle-derived 'arc-related' magmas. Physics of the Earth and Planetary Interiors 127, 215–232.

Ulrich, M., Picard, C., Guillot, S., Chauvel, C., Cluzel, D., Meffre, S., 2010. Multiple melting stages and refertilization as indicators for ridge to subduction formation: the New Caledonia ophiolite. Lithos 115, 223–236.

Walker, R.J., Hanski, E., Vuollo, J., Liipo, J., 1996. The Os isotopic composition of Proterozoic upper mantle: evidence for chondritic upper mantle from the Outokumpu ophiolite, Finland. Earth and Planetary Science Letters 141, 161–173.

1186 Wang, Z., Becker, H., 2013. Ratios of S, Se and Te in the silicate Earth require a
1187 volatile-rich late veneer. Nature 499, 328–331.

1188 Wang, Z., Becker, H., Gawronski, T., 2013. Partial re-equilibration of highly
1189 siderophile elements and the chalcogens in the mantle : A case study on the
1190 Baldissero and Balmuccia. Geochimica et Cosmochimica Acta 108, 21–44.

1191 Whattam, S. A., 2009. Arc-continent collisional orogenesis in the SW Pacific and the
1192 nature, source and correlation of emplaced ophiolitic nappe components. Lithos 113,
1193 88–114.

1194 Widom, E., Kepezhinskas, P., and Defant, M., 2003, The nature of metasomatism in
1195 the sub-arc mantle wedge: Evidence from Re-Os isotopes in Kamchatka peridotite
1196 xenoliths: Chemical Geology 196, 283–306.

1197 Widom, E., 2011. Recognizing recycled Osmium. Geology 39, 1087–1088.

1198 Wood, B.J., Virgo, D., 1989. Upper mantle oxidation state: ferric iron contents of
1199 lherzolite spinels by 57Fe Mössbauer spectroscopy and resultant oxygen fugacities.
1200 Geochimica et Cosmochimica Acta 53, 1277–1291.

1201 Woodland, A.B., Kornprobst, J., Tabit., A., 2006. Ferric iron in orogenic lherzolite
1202 massifs and controls of oxygen fugacity in the upper mantle. Lithos 89, 222-241.

1203

1204 Figure captions

1205 Fig. 1. a) Present-day structures of the Southwest Pacific region modified after Cluzel
1206 et al. (2012). Dark orange, land; light orange, continental plateau; white, oceanic
1207 basins (LHR: Lord Howe Rise, NR: Norfolk ridge, LR: Loyalty ridge, HP: Hikurangi
1208 Plateau); b) simplified geological map of New Caledonia showing distribution of the
1209 Peridotite massifs (modified after Cluzel et al., 2012).

Fig. 2. Variations of Os, Ru, Rh, Pt, Pd, Au and Re vs. Ir for the New Caledonia peridotites. Abyssal peridotites (Kane fracture zone: Snow and Schmidt, 1998; Brandon et al., 2000; Luguet et al., 2001, 2003; Marchesi et al., 2013; MAR: Harvey et al., 2006; Lena trough: Lassiter et al., 2014) and ophiolitic peridotites (IL-EL: Internal and External Ligurides, Snow et al., 2000; Luguet et al., 2004; Fischer-Godde et al., 2011; Lanzo: Becker et al., 2006; Pyrenees: Becker et al., 2006; Luguet et al., 2007) are shown for comparison.

Fig. 3. Primitive mantle normalised HSE and chalcogen patterns for the New Caledonia spinel and plagioclase lherzolites. Grey shaded area includes oceanic lherzolites from Mid-Atlantic and South West Indian ridges (Snow and Schmidt, 1998; Luguet et al., 2001; Luguet et al., 2003) and ophiolitic lherzolites from the Ligurian Units (Snow et al., 2000; Luguet et al., 2004; Fischer-Gödde et al. 2011). Normalising values after Becker et al. (2006), Fischer-Gödde et al. (2011) and Wang and Becker (2013).

Fig. 4. a) Al_2O_3 (wt.%)-$^{187}Os/^{188}Os_i$ and b) Os-$^{187}Os/^{188}Os_i$ and c) $^{187}Re/^{188}Os$-$^{187}Os/^{188}Os$ diagrams showing data from New Caledonia lherzolites and type-A harzburgites in comparison to PM compositions. PM data from Meisel et al. (1996). Data for abyssal peridotites are from Harvey et al., (2006) for Atlantic peridotites, Lassiter et al., (2014) for Lena through and Liu et al. (2015) for Gakkel ridge. See Fig. 2 for ophiolitic peridotites references.

1233 Fig. 5. a) Te vs. Se, b) Te vs. Pd and c) S vs. S/Se correlation diagrams for New
1234 Caledonia spinel and plagioclase lherzolites. Data for orogenic lherzolites from Wang
1235 and Becker (2013) are also plotted for comparison.

1236

1237 Fig. 6. a) Primitive mantle normalised HSE and chalcogen abundances in type-A
1238 harzburgites. Light grey shaded field encompasses the area of modern MOR
1239 harzburgites (Snow and Schmidt, 1998; Luguet et al., 2001, 2003; Harvey et al.,
1240 2006; Marchesi et al., 2013); b) Primitive mantle normalised diagram showing HSE
1241 and chalcogen patterns of type-B harzburgites. Normalising values are after Becker et
1242 al. (2006), Fischer-Gödde et al. (2011) and Wang and Becker (2013).

1243

1244 Fig. 7. a) $Fe^{3+}/\Sigma Fe$ ratios in spinel and b) $\log(f_{O2})$ ΔFMQ vs Cr# in spinel for samples
1245 from this study. Error bars in a = relative error expressed as % (see Table 2). Error
1246 for $\log(f_{O2})$ ΔFMQ includes error related to f_{O2} sensor (0.5 log units) plus uncertainties
1247 derived from Fe^{3+}/Fetotal ratio measurements (see Table 2).
1248 Background fields represent literature data for mantle peridotites: pink= abyssal
1249 peridotites (Bryndzia and Wood, 1990); grey = arc xenoliths (Wood and Virgo, 1989;
1250 Brandon and Draper, 1996; Parkinson et al., 2003); light green and light yellow =
1251 Toroshima and Conical seamount respectively (Parkinson and Pearce, 1998). Modified
1252 after Birner et al. (2017).

1253

1254 Fig. 8. Primitive mantle normalised HSE abundances of a) type-A and b) type-B
1255 harzburgites compared to the HSE composition displayed by New Zealand mantle
1256 xenoliths (Scott et al., 2019). See text for further detail.

1257

Figure 1

Click here to download high resolution image

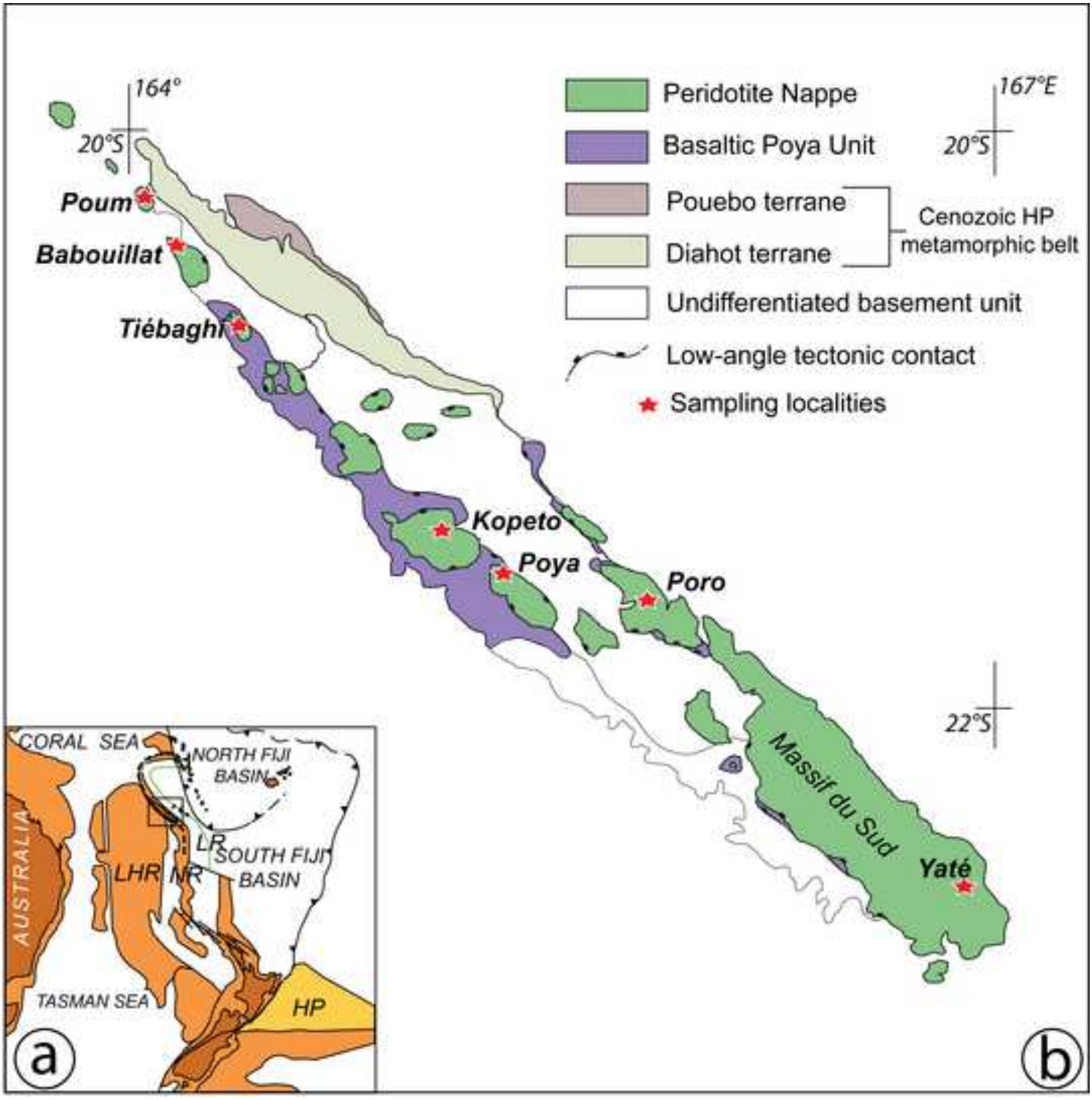

Figure 2

Click here to download high resolution image

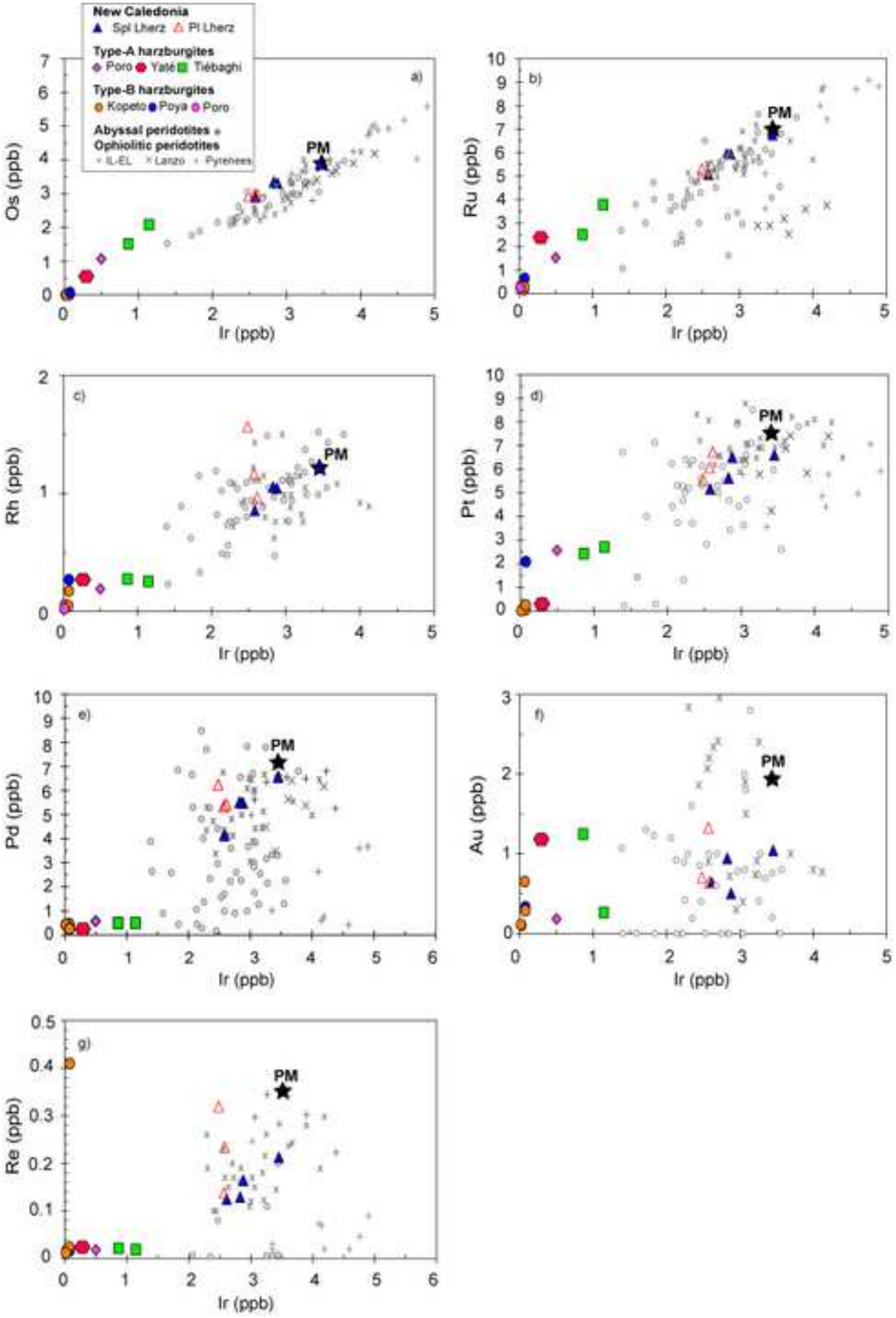

Figure 3

Click here to download high resolution image

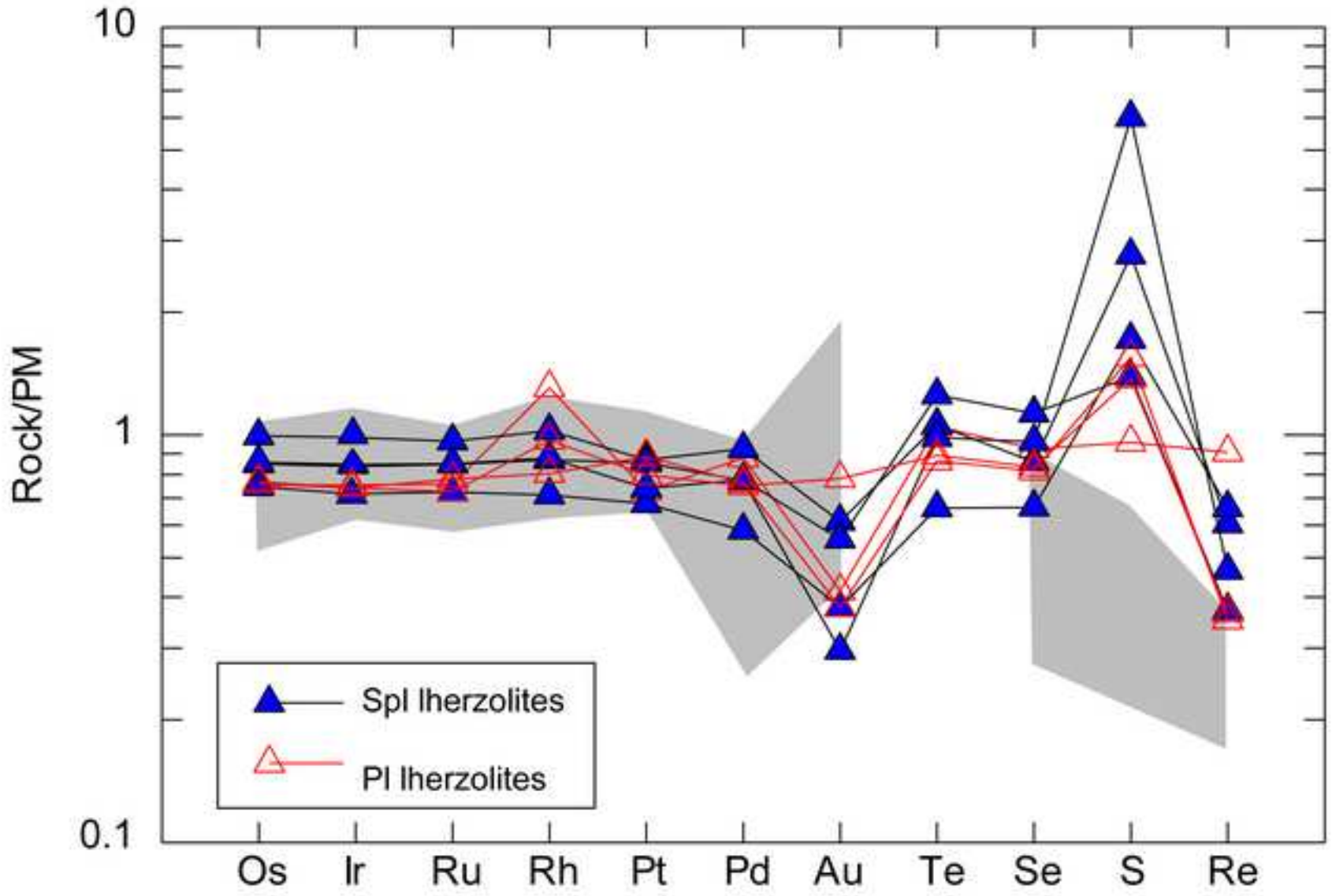

Figure 4

Click here to download high resolution image

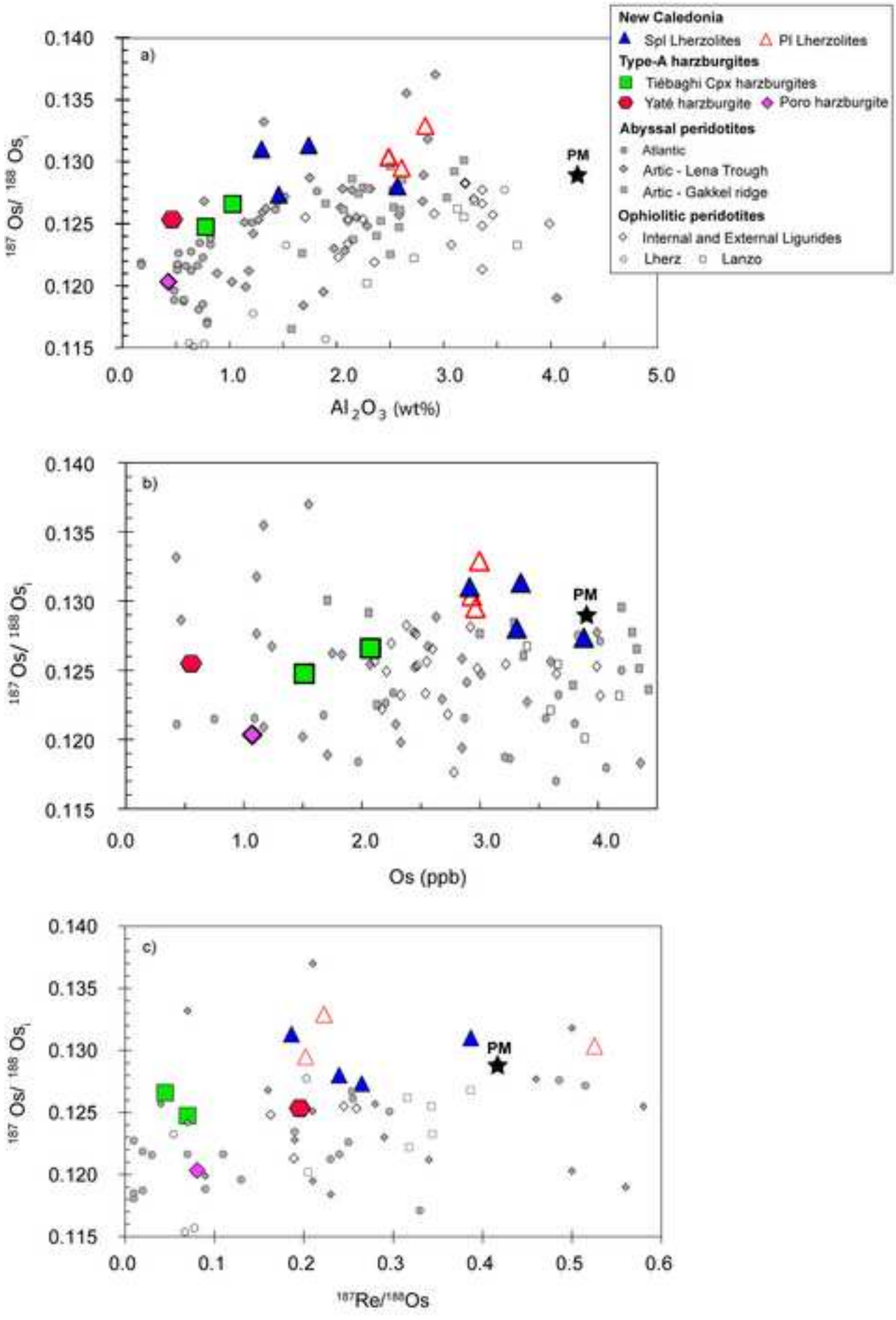

Figure 5

Click here to download high resolution image

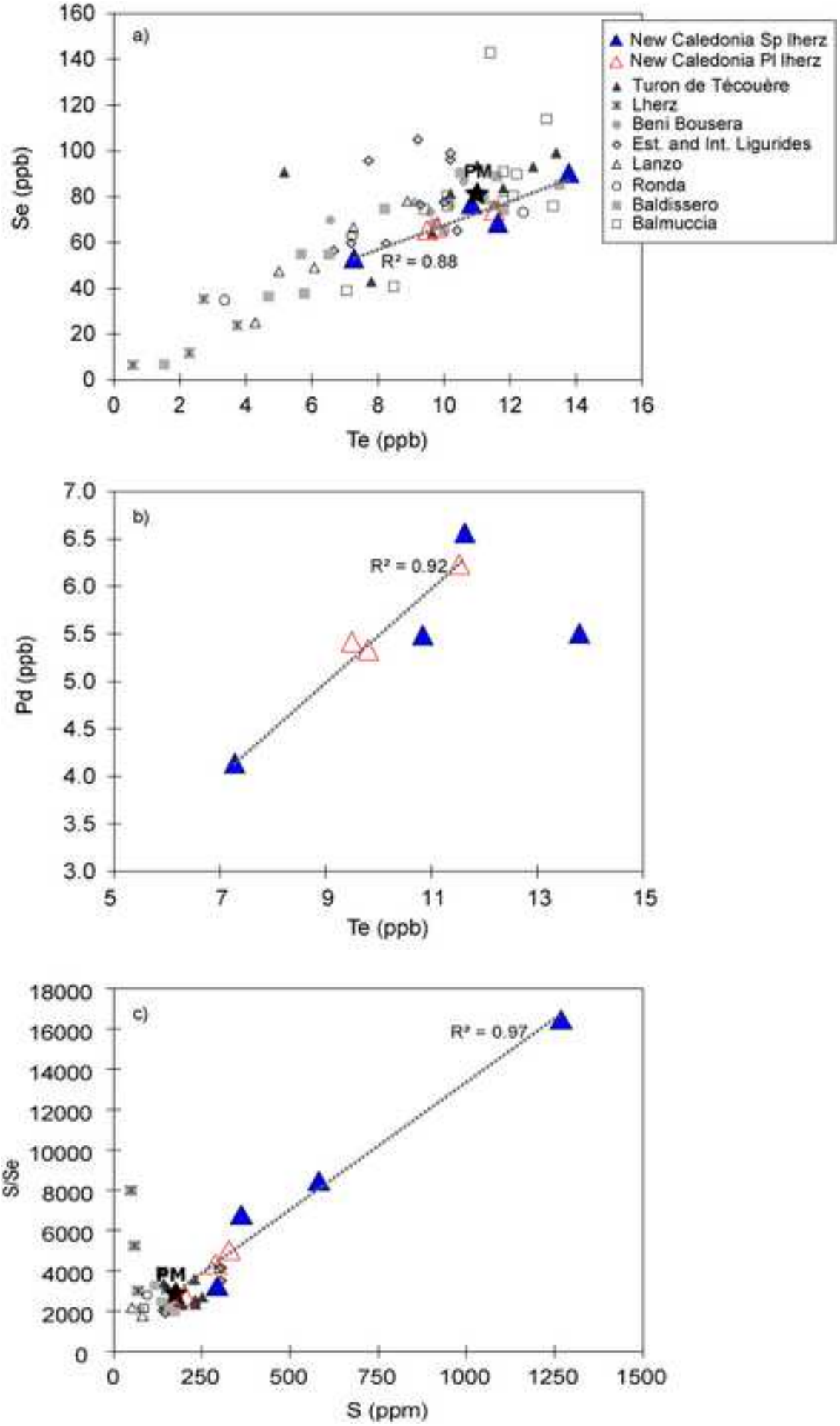

Figure 6

Click here to download high resolution image

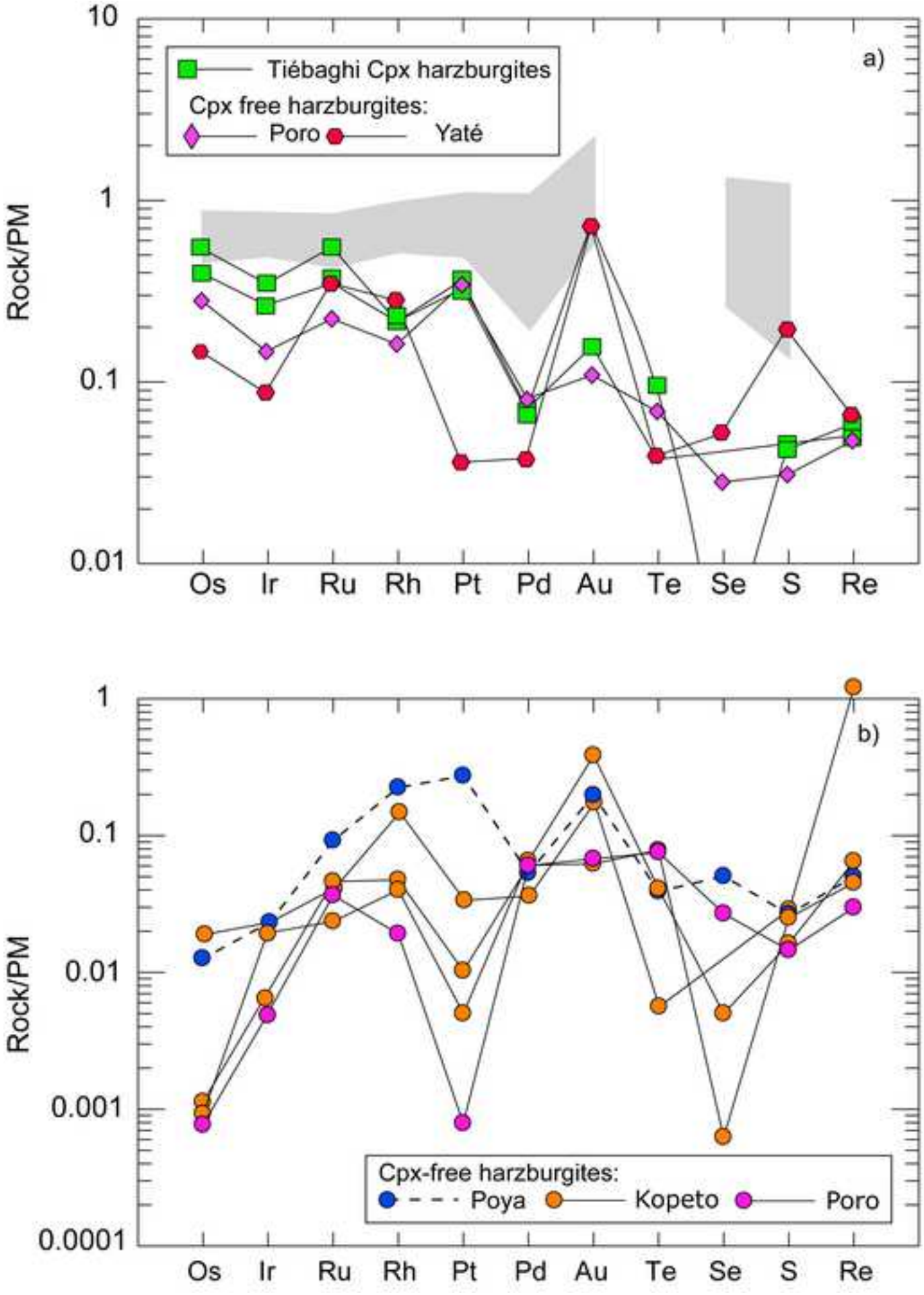

Figure 7

Click here to download high resolution image

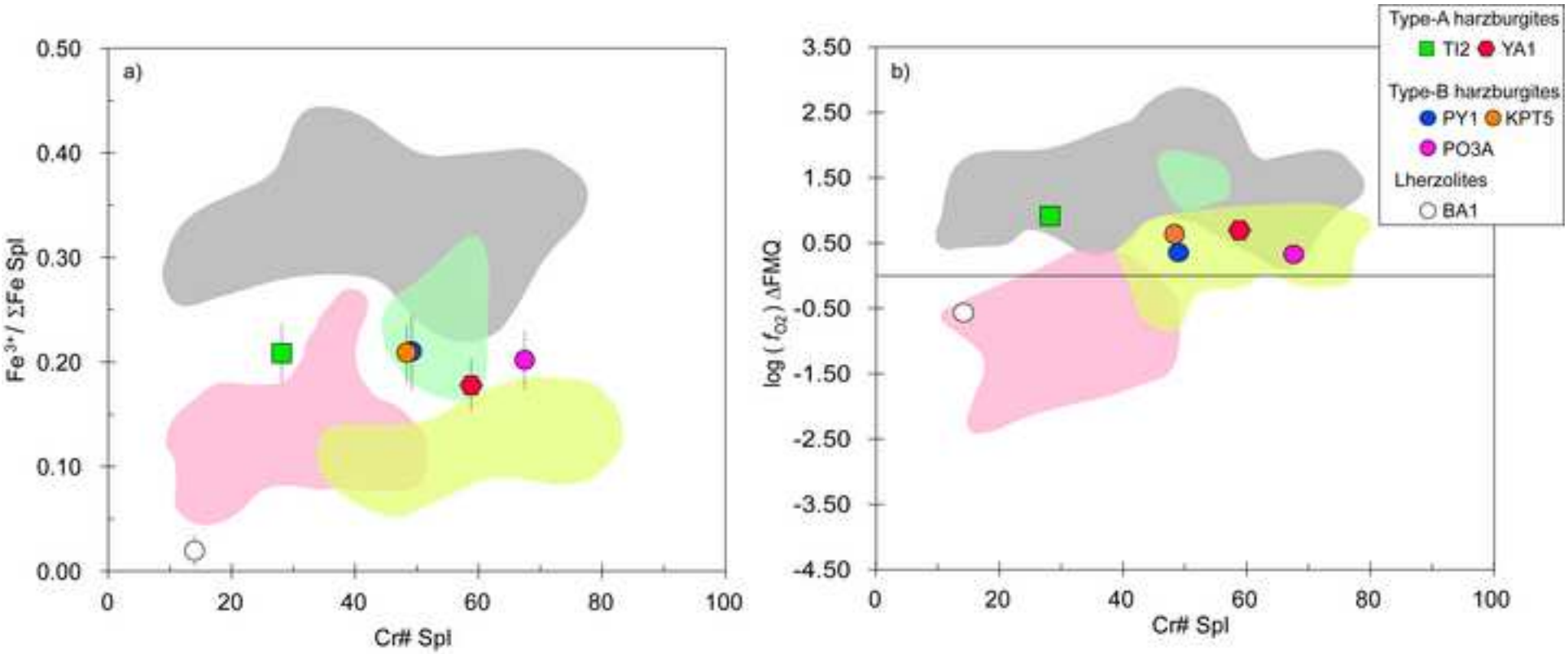

Figure 8

Click here to download high resolution image

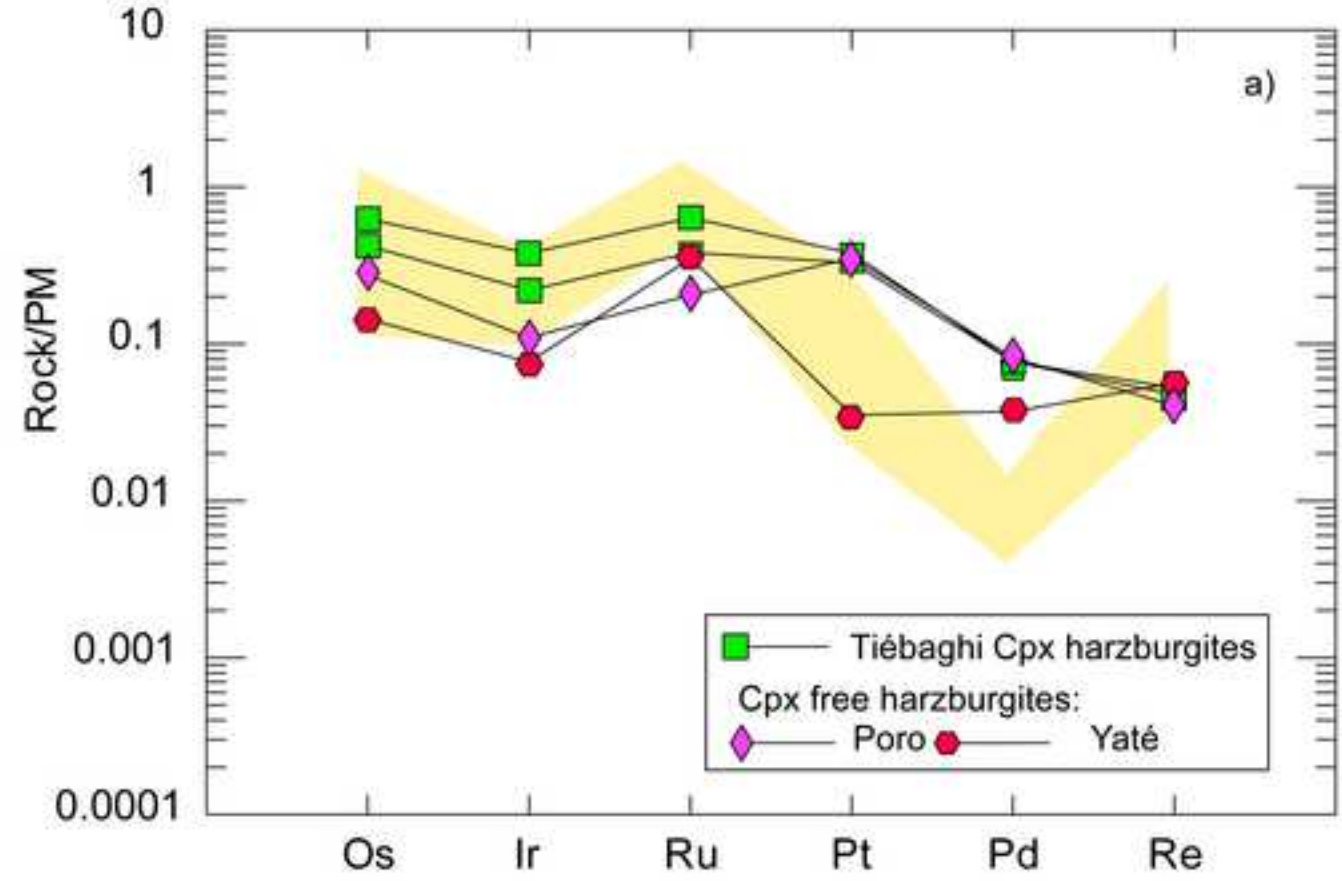

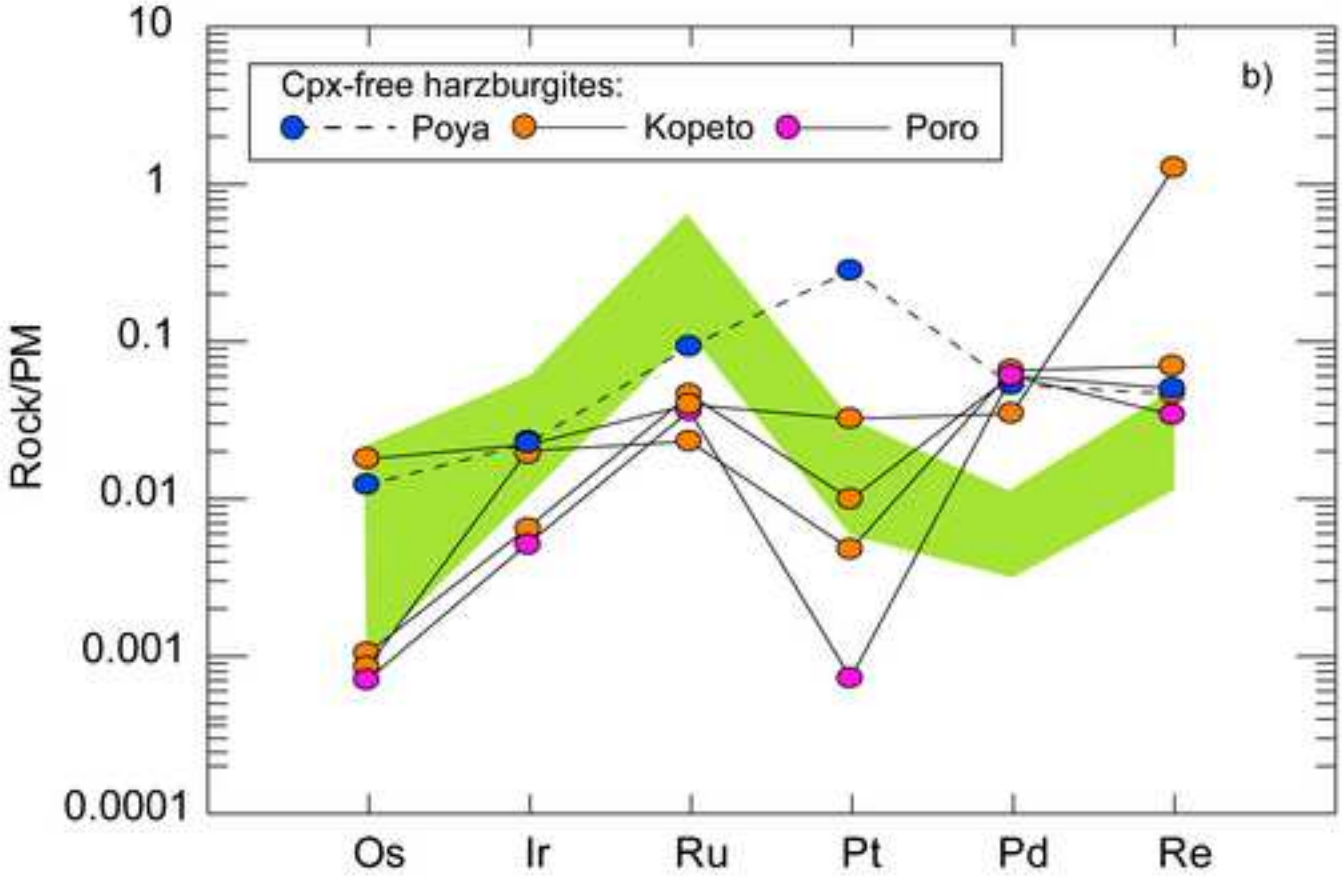

Figure S1
Click here to download high resolution image

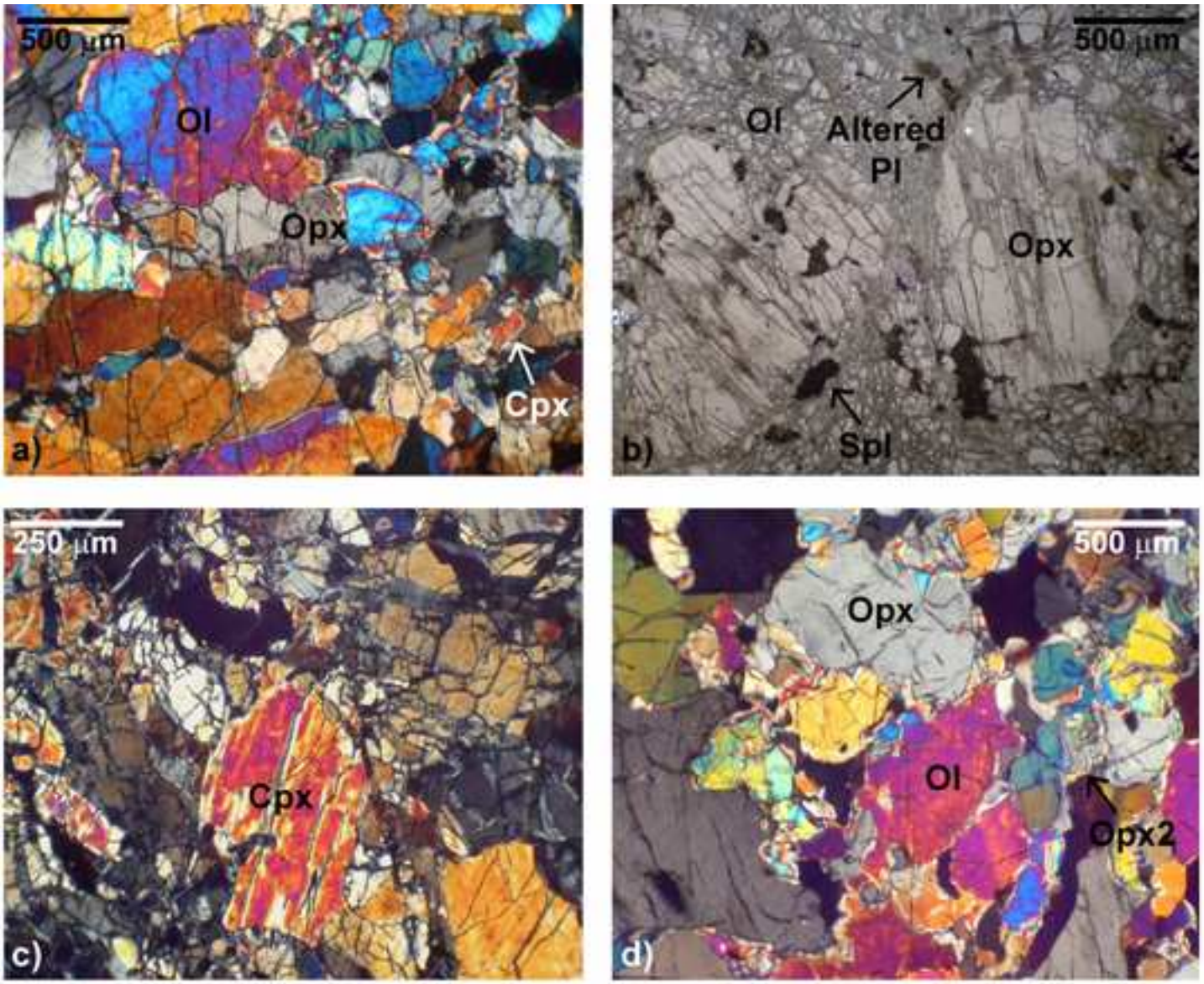

Microphotographs of the New Caledonia peridotites: a) porphyroclastic texture marked by deformed and stretched olivine and orthopyroxene crystals in spl-lherzolite POU2; b) plagioclase-lherzolite thin section (BAB2A, parallel polars); c) strongly exsolved, primary clinopyroxene occurrence in TI2 harzburgite; d) interstitial orthopyroxene (opx2) formed at the expense of primary olivine (KPT5 harzburgite).

Figure S2

Click here to download high resolution image

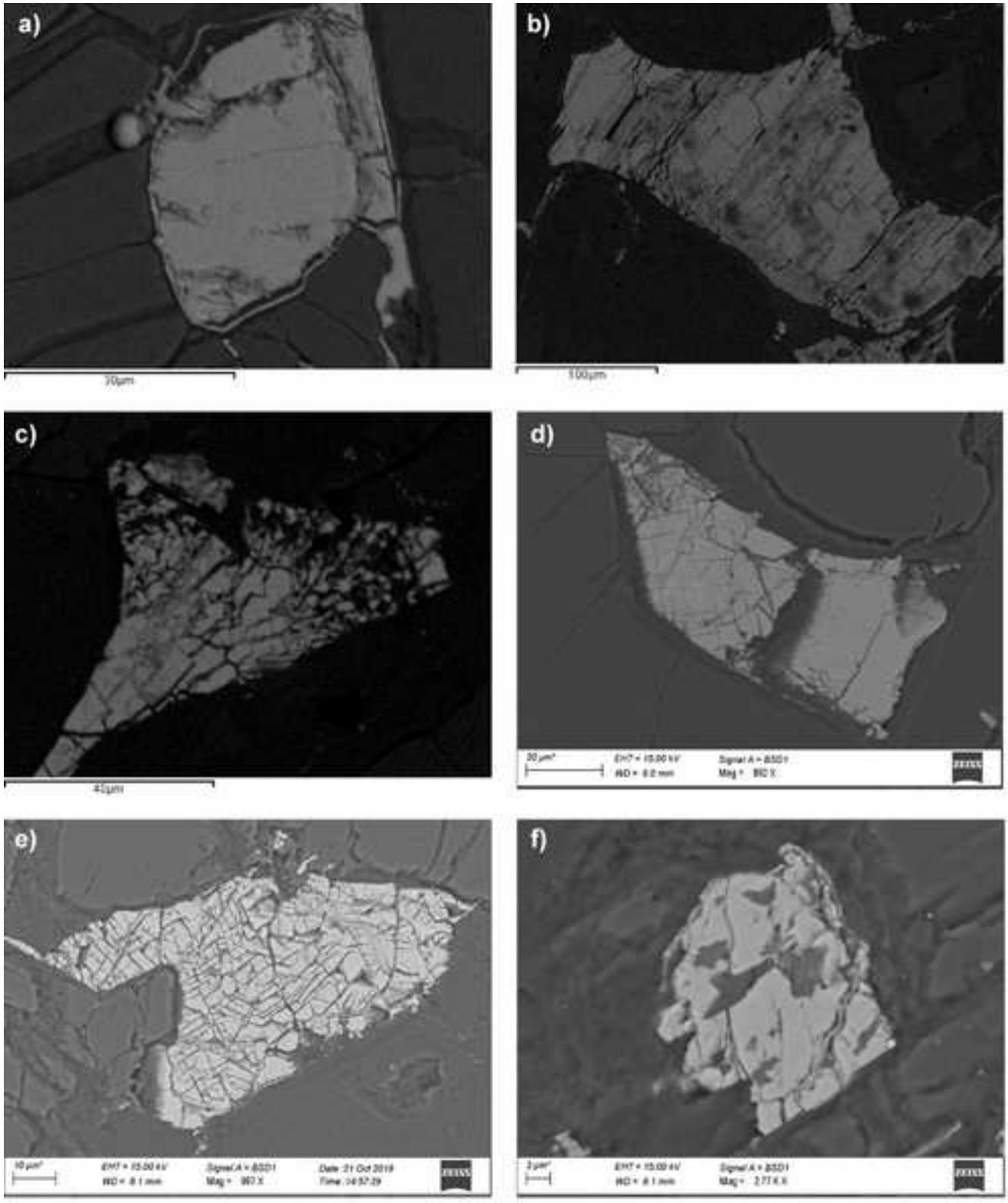

BSE images of sulphide phases in the New Caledonia lherzolites: a) small, rounded, interstitial sulphide in BA1 (Mss); b-c) sulphide grains included in porphyroclastic olivine (POU2 lherzolite, b= pentlandite, c= Mss); d) irregular-shaped, interstitial, Mss grain (BAB1B); e) interstitial sulphide (pentlandite, POU3); f) Mss grain enclosed in olivine (POU1A).

Figure S3

Click here to download high resolution image

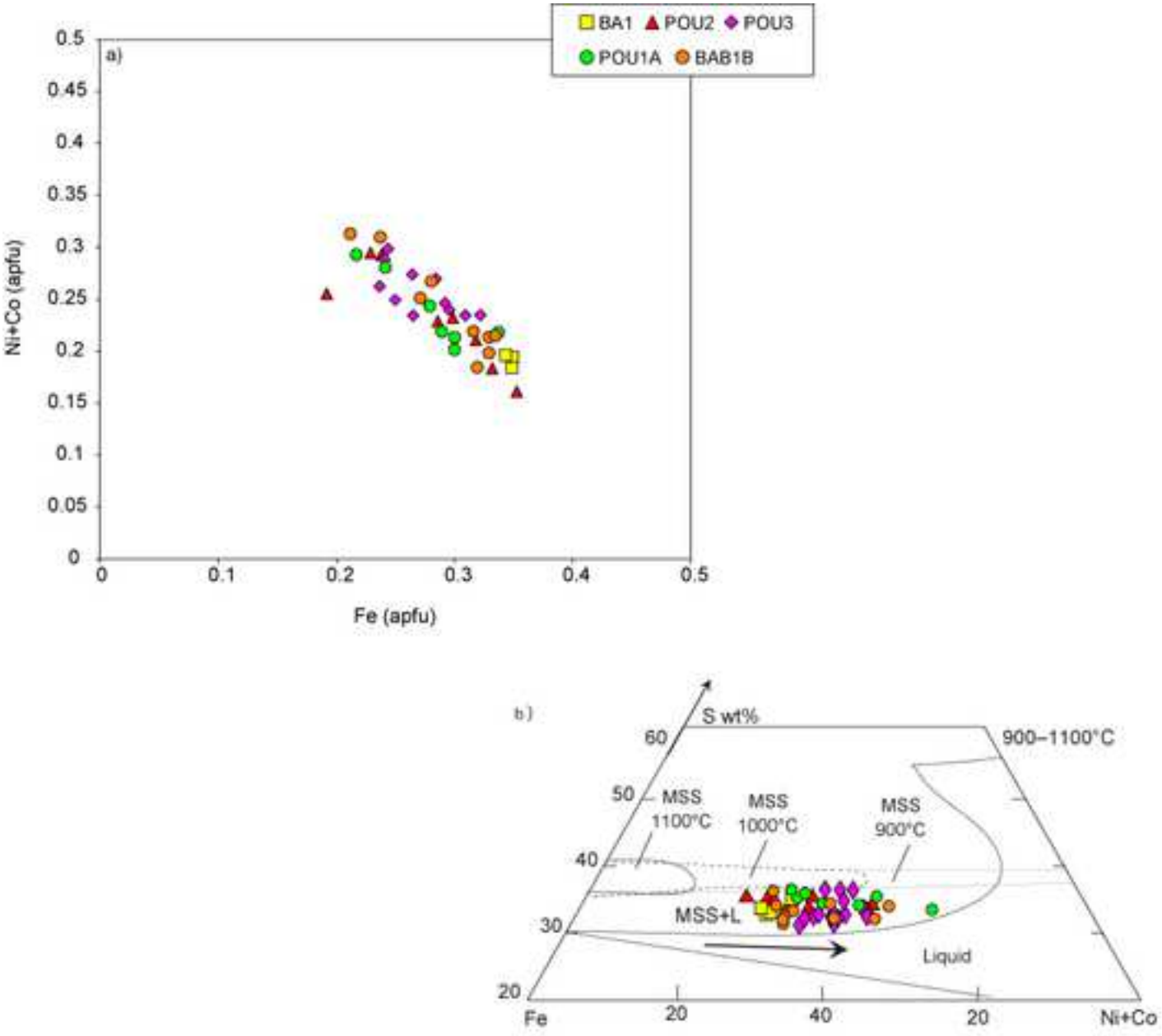

Fig. S3. a) Plot of Fe (at%) v. (Ni + Co) (at %) showing compositional variations of sulphides in the New Caledonia lherzolites; b) projection in the Fe-(Ni +Co)-S system of sulphide compositions. Phase relations from Kullerud et al. (1969) and Craig (1973).

Figure S4

Click here to download high resolution image

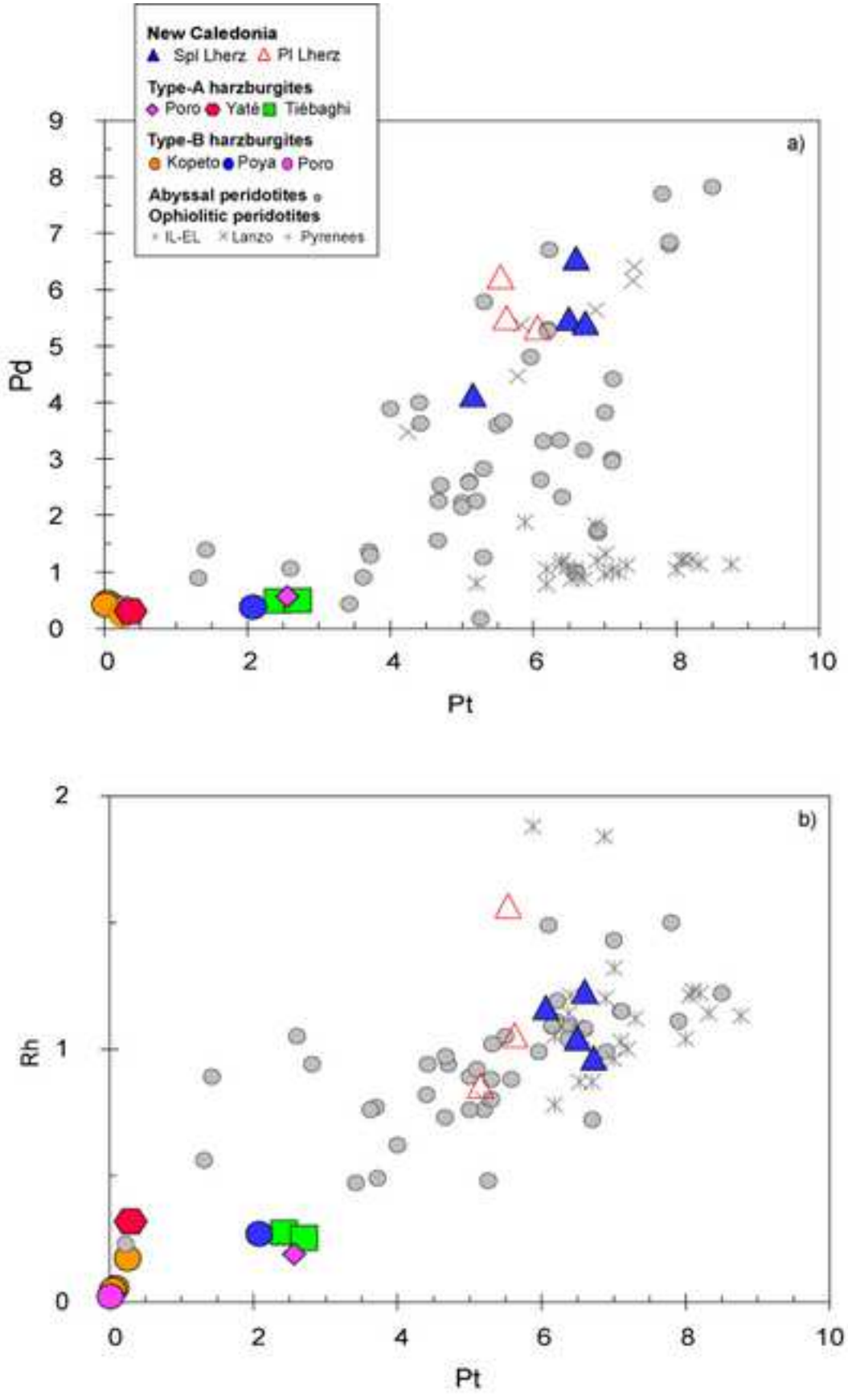

Pt vs. a) Pd and b) Rh variation diagrams for the New Caledonia peridotites. Abundances are in ppb.

Table 1

Click here to download Table: Table 1.xlsx

Table 1

Concentrations of the HSE, S, Se and Te, Os isotopes, selected major elements and ratios for the New Caledonia peridotites

Sample	Rock	Al_2O_3 *wt.%*	LOI %	Os *(ng/g)*	Ir *(ng/g)*	Ru *(ng/g)*	Rh *(ng/g)*	Pt *(ng/g)*	Pd *(ng/g)*	Au *(ng/g)*	Re *(ng/g)*	Os_N/Ir_N	Os_N/Ru_N	Pd_N/Ir_N	Ru_N/Ir_N	Pt_N/Ir_N	Pt_N/Ru_N	$^{187}Re/^{188}Os$ (2SE)	$^{187}Os/^{188}Os$ *measured*	2SE	$^{187}Os/^{188}Os_i$	$\gamma Os_{(53Ma)}$	T_{MA} (PM) *Ga*	T_{RD} (PM) *Ga*	T_{RD2} (PM) *Ga*	S (µg/g)	Se *(ng/g)*	Te *(ng/g)*	S/Se	Se/Te
POU1A	Pl L	2.49	7.56	2.93	2.48	5.31	1.57	5.54	6.23	0.704	0.319	1.06	0.99	1.24	1.07	1.03	0.96	0.525(1)	0.130822	9.1E-06	0.130358	2.9	0.8	f	f	202	74.9	11.5	2703	6.5
POU2	Sp L	1.46	8.63	3.88	3.45	6.76	1.23	6.60	6.56	1.04	0.213	1.01	0.18	0.94	5.71	0.88	0.15	0.265(1)	0.127574	6.8E-06	0.127340	0.5	0.7	f	0.3	582	69.6	11.6	8364	6.0
POU2B	Sp L	2.57	10.69	3.31	2.88	5.93	1.04	6.49	5.49	0.503	0.165	1.03	1.09	0.94	0.95	1.04	1.09	0.240(1)	0.128227	8.0E-06	0.128016	1.1	0.4	f	0.2	1268	77.8	10.8	16289	7.2
POU3	Sp L	1.30	9.60	2.91	2.58	5.07	0.86	5.15	4.14	0.642	0.234	1.01	1.05	0.79	0.97	0.92	0.95	0.387(1)	0.131356	9.1E-06	0.131015	3.4	f	f	f	362	54.0	7.3	6691	7.4
BA1	Sp L	1.74	6.39	3.34	2.85	5.95	1.05	5.62	5.51	0.943	0.129	1.06	0.27	0.96	3.88	0.92	0.24	0.186(1)	0.131485	7.9E-06	0.131320	3.7	f	f	f	294	91.3	13.8	3218	6.6
BAB1B	Pl L	2.61	6.98	2.96	2.61	5.46	0.965	6.73	5.42	0.641	0.125	1.02	0.24	1.02	4.30	1.19	0.28	0.202(1)	0.129664	8.9E-06	0.129485	2.2	f	f	0.0	327	66.2	9.5	4943	7.0
BAB2B	Pl L	2.83	8.43	3.00	2.57	5.08	1.16	6.06	5.33	1.33	0.138	1.05	1.67	1.02	0.63	1.09	1.73	0.223(1)	0.133084	8.9E-06	0.132887	4.9	f	f	f	289	67.6	9.8	4278	6.9
TI1	H	0.78	9.01	1.51	0.864	2.52	0.275	2.42	0.488	1.25	0.022	1.57	1.08	0.28	1.46	1.29	0.89	0.070(25)	0.12479	1.7E-05	0.12473	-1.5	0.8	0.7	0.7	9	1.1	1.0	8188	1.0
TI2	H	1.03	6.04	2.07	1.14	3.78	0.254	2.70	0.499	0.264	0.019	1.63	0.98	0.21	1.65	1.09	0.66	0.045(18)	0.12662	1.3E-05	0.12658	-0.1	0.5	0.4	0.4	10	0.7	0.4	14053	1.7
PO4	H	0.43	0.18	1.07	0.499	1.53	0.191	2.56	0.570	0.160	0.018	1.93	1.26	0.56	1.53	2.36	1.54	0.081(35)	0.12040	2.4E-05	0.12033	-5.0	1.5	1.3	1.3	6	3.1	0.8	2084	4.1
YA1	H	0.46	6.83	0.554	0.297	2.35	0.326	0.268	0.263	1.17	0.022	1.67	0.42	0.44	3.95	0.42	0.11	0.196(68)	0.12551	4.7E-05	0.12534	-1.0	1.0	0.6	0.6	40	4.9	0.4	8117	11.4
PY1	H	0.78	0.00	0.049	0.077	0.643	0.269	2.08	0.378	0.336	0.016	0.58	0.14	2.43	4.19	2.97	2.97	1.62(8)	0.1299	5.3E-04	0.1284	1.4	0.0	0.0	0.2	6	0.9	0.9	6103	1.1
Duplicate				0.023	0.133	0.693	0.171	2.44	0.588	0.311	0.062							13.0(1)	0.127	1.0E-03	0.115	-8.9				53	0.3	1.0	196197	0.3
KPT2	H	0.70	3.03	0.004	0.022	0.323	0.057	0.078	0.431	0.107	0.018	0.18	0.02	9.50	7.22	0.22	0.22	19(1)	0.148	5.6E-03	0.131	3.6	0.1	f	f	5	1.3	0.4	4164	2.8
Duplicate				0.036	0.017	0.211	0.040	0.210	0.620	0.144	0.010							1.4(1)	0.302	1.3E-03	0.301	137.8				7	1.3	8.2	4947	0.2
KPT5	H	0.74	0.12	0.004	0.066	0.165	0.048	0.038	0.464	0.654	0.024	0.05	0.04	3.46	1.25	0.21	0.21	32(2)	0.147	6.2E-03	0.118	-6.6	0.0	f	f	3	3.0	0.7	1133	4.1
Duplicate				0.007	0.062	0.165	0.054	0.046	0.512	0.603	0.056							37(1)	0.160	3.2E-03	0.127	0.5				3	0.7	1.3	4453	0.5
PO3	H	0.41	0.00	0.003	0.015	0.256	0.023	0.006	0.428	0.084	0.012	0.18	0.02	14.12	8.57	0.02	0.02	19(2)	0.153	8.4E-03	0.136	8.0	0.1	f	f	3	1.4	0.6	2129	2.2
Duplicate				0.055	0.018	0.243	0.016	0.009	0.573	0.293	0.0078							0.69(7)	0.1239	4.7E-04	0.1233					bdl	bdl	0.8	-	-
KPT3	H	0.67	0.67	0.072	0.079	0.280	0.172	0.248	0.250	0.288	0.410	0.81	1.87	0.17	0.19	6.92	6.92	28(1)	0.1273	3.5E-04	0.1204	-5.1	0.0	0.3	1.3	6	bdl	bdl	-	-

Duplicate: replicate digestion of the same sample powder

Pl L= plagioclase lherzolite, Sp L= spinel lherzolite, H= harzburgite

Values of PM $^{187}Os/^{188}Os$ = 0.1296 and $^{187}Re/^{188}Os$ = 0.434 used for calculation of T_{MA} and T_{RD} ages (Meisel et al., 2001); f= future model ages. T_{RD2} (PM) indicates depletion ages calculated taking into account Re addition that may have occurred during peridotite evolution.

Table 2

Click here to download Table: Table 2.xlsx

Table 2

Equilibration temperature, pressure, and oxygen fugacity calculated for selected peridotite samples. Average spinel compositions are also reported.

Sample	Type	$Fe^{3+}/\Sigma Fe$[1]	$Fe^{3+}/\Sigma fe$ (rel. err.%)[2]	T Ol-Spl (°C)[3]	P (GPa)	Wood[4] (1990)	
						log *f(O2)*	ΔFMQ
TI2	Type-A harz	0.21 (0.03)	15.0	870	1.0	-11.37	0.92
YA1	Type-A harz	0.18 (0.03)	14.5	815	1.0	-12.66	0.67
KPT5	Type-B harz	0.21 (0.03)	16.0	840	1.0	-12.20	0.65
PO3A	Type-B harz	0.20 (0.03)	14.8	940	1.0	-10.76	0.33
PY1B	Type-B harz	0.21 (0.03)	16.6	930	1.0	-10.90	0.35

		Spinel											
Sample	Type	SiO_2	TiO_2	Al_2O_3	Cr_2O_3	FeO	Fe_2O_3	MnO	MgO	Total	Cr#	Mg#	$L\beta/L\alpha$[5]
TI2	Type-A harz	0.04	0.03	43.45	25.35	10.20	2.99	0.15	16.93	99.13	0.281	0.747	0.804
YA1	Type-A harz	0.02	0.01	21.56	45.88	16.76	4.03	0.29	10.81	99.35	0.588	0.535	0.896
KPT5	Type-B harz	0.01	0.01	29.66	41.41	11.31	3.31	0.21	14.41	100.33	0.484	0.695	0.825
PO3A	Type-B harz	0.02	0.00	17.27	53.48	12.58	3.54	0.25	12.32	99.47	0.675	0.636	0.833
PY1B	Type-B harz	0.01	0.01	29.35	41.87	11.20	3.32	0.20	14.42	100.38	0.492	0.696	0.826

[1] $Fe^{3+}/(Fe^{2+}+Fe^{3+})$ in spinel determined by "flank"-method.

$Fe^{3+}/(Fe^{2+}+Fe^{3+})$ ratio has been calculated using the equation : $L\alpha/L\beta$ x 0.42+ Cr# x 0.03 - (FeO + (Fe_2O_3/1.113)) x 0.01 obtained after standardisation.

[2] Relative error in % calculated as a total of measurement errors for Fe, Cr, Al and X-ray intensities at flank positions.

[3] T Ol-Spl = Equilibration temperature calculated using Li et al. (1995) formulation.

[4] Oxygen fugacity estimates are from Wood et al. (1990) and are reported as Δlog fO2 from the quartz-fayalite-magnetite (FMQ) buffer using the $Fe^{3+}/\Sigma Fe$ values of the analysed spinels. See text for further details.

[5] Current normalized ratio of the intensities at flank position for $L\alpha$ and $L\beta$ Fe lines

Table S1

Click here to download Table: Table S1.xlsx

Table S1

Major element composition for selected sulphides from the New Caledonia lherzolites

Sample	POU2	POU2	POU2	POU2	POU2	POU2	POU2	BA1	BA1	BA1	BA1	BA1
Mineral	*mss*	*mss*	*mss*	*pn*	*pn*	*pn*	*pn*	*mss*	*mss*	mss	*mss*	*mss*
Occurrence	*Encl*	*Interst*	*Encl*	*Encl*	*Interst*	*Interst*	*Interst*	*Interst*	*Interst*	*Interst*	*Encl*	*Encl*
wt%												
S	34.32	34.39	32.74	33.24	41.19	32.68	40.82	33.22	33.08	32.47	32.53	33.13
Fe	41.23	43.80	36.65	28.09	23.90	29.14	24.68	36.85	42.99	43.25	42.19	43.02
Co	0.64	0.59	0.78	0.46	1.93	1.91	2.26	0.46	0.50	0.55	0.80	0.58
Ni	23.28	20.44	29.19	37.55	32.99	35.74	32.23	25.77	23.44	24.72	24.54	23.27
Cu	0.52	0.57	0.64	0.66	bdl	0.53	bdl	3.70	bdl	bdl	bdl	bdl
Total	99.99	99.79	100.00	100.00	100.01	100.00	99.99	100.00	100.01	100.99	100.06	100.00
Fe/Ni	1.8	2.1	1.3	0.7	0.7	0.8	0.8	1.4	1.8	1.7	1.7	1.8

Interst. =interstitial; encl = enclosed

Pn= pentlandite; mss= monosulphide solid solution

Table S2

Click here to download Table: Table S2.xlsx

Average major element composition of olivine from the analysed harzburgites

Sample	Type	SiO_2	FeO	MnO	MgO	NiO	Total	Mg#
TI2	Type-A harz	41.79	7.96	0.25	49.88	0.51	100.39	0.918
YA1	Type-A harz	41.39	8.14	0.24	50.03	0.37	100.16	0.914
KPT5	Type-B harz	41.83	7.54	0.23	50.01	0.47	100.07	0.923
PO3A	Type-B harz	41.56	8.60	0.08	49.54	0.41	100.19	0.914
PY1B	Type-B harz	41.34	8.26	0.09	50.25	0.33	100.27	0.915

Average major element composition of orthopyroxene from the analysed harzburgites

Sample	Type	SiO_2	Al_2O_3	Cr_2O_3	FeO	MnO	MgO	CaO
TI2	Type-A harz	55.69	4.13	0.87	6.03	0.18	32.93	0.56
YA1	Type-A harz	57.51	1.42	0.76	5.01	0.09	34.32	0.90
KPT5	Type-B harz	57.16	1.91	0.71	5.17	0.18	34.01	0.88
PO3A	Type-B harz	57.98	0.94	0.44	5.70	0.25	34.88	0.35
PY1	Type-B harz	57.22	2.37	0.96	5.47	0.10	33.63	0.71